Marine Geology 472 (2024) 107301

Contents lists available at ScienceDirect

Marine Geology

journal homepage: www.elsevier.com/locate/margo

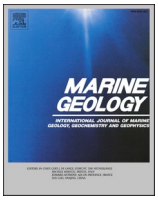

Late-Pleistocene rejuvenated volcanism and flank collapse deposits on a Cretaceous seamount near El Hierro, Canary Archipelago

Andreas Klügel [a,*], Folkmar Hauff [b], Christoph Beier [c], Jörg A. Pfänder [d], Armin Freundt [b], Miriam Römer [a,e], Milena Schönhofen-Romer [f]

[a] Fachbereich Geowissenschaften, Universität Bremen, Postfach 330440, 28334 Bremen, Germany
[b] GEOMAR Helmholtz-Zentrum für Ozeanforschung Kiel, Wischhofstr. 1-3, 24148 Kiel, Germany
[c] Department of Geosciences and Geography, Research Programme of Geology and Geophysics (GeoHel), University of Helsinki, PO Box 64, FIN-00014, Finland
[d] Institut für Geologie, Technische Universität Bergakademie Freiberg, Bernhard-von-Cotta Str. 2, 09599 Freiberg, Germany
[e] MARUM - Center for Marine Environmental Sciences, Universität Bremen, Postfach 330440, 28334 Bremen, Germany
[f] GeoZentrum Nordbayern, Friedrich-Alexander Universität Erlangen-Nürnberg, Schlossgarten 5, 91054 Erlangen, Germany

ARTICLE INFO

Editor: Natascha Riedinger

Keywords:
Seamount
Intraplate volcanism
Rejuvenated volcanism
Flank collapse
Canary Islands
Atlantic

ABSTRACT

Henry Seamount is a Cretaceous submarine volcano located 40 km southeast of El Hierro, the youngest of the Canary Islands, at 3700 m water depth. On the seamount's summit region, a widespread layer of heterolithologic volcaniclastic ash and lapilli beneath centimeters to decimeters of pelagic sediment was discovered and sampled during R/V *Meteor* cruise 146. The dominant lithology is a glassy basaltic ash that is depleted in highly incompatible elements and enriched in sulfur (S/K_2O ratios of 0.10–0.20) compared to El Hierro lavas, suggesting an origin by a deep-sea volcanic eruption on Henry Seamount. Uranium-series disequilibria constrain the age of this ash to <350 ka, which implies rejuvenated volcanic activity of the seamount after up to 126 Ma of dormancy. This rejuvenated activity is possibly related to the Canary hotspot, where heating of lithosphere that had become amphibole-metasomatized during the formation of Henry Seamount led to renewed melt production. In contrast to the dominant ash type, most other volcaniclastic samples are geochemically indistinguishable from El Hierro lavas. The variety of lithologies, the angular to edge-rounded shapes of many fragments, and intimate mixture with the predominant ash suggest that this group of volcaniclastics was transported from El Hierro to Henry Seamount by a submarine debris avalanche and associated turbidity current. This implies a runup of up to 700 m even for centimeter-sized basaltic clasts after up to 40 km of lateral transport. Ar—Ar age constraints for two samples are ~190–200 ka, which is consistent with the southeast-directed giant Las Playas II landslide from El Hierro as the most likely source. Henry Seamount thus provides a rare example where collapse-induced deposits from another volcanic edifice are found on top of a seamount and are mingled with ash to lapilli from previous rejuvenated volcanism. Mingling and reworking of the tephra may explain the lack of a discernible eruption center on top of the seamount.

1. Introduction

The seafloor is scattered with hundreds of thousands of volcanic seamounts that occur in all parts of the ocean plates (Wessel, 2001; Hillier and Watts, 2007). Intraplate seamounts are principal constituents of volcanic island archipelagos, but also occur as solitary edifices without apparent relation to hotspot volcanism. Many intraplate solitary seamounts occur in the eastern central Atlantic off NW-Africa, which includes the Canary Island Seamount Province and the Canary Basin (van den Bogaard, 2013; Medialdea et al., 2017). Some of them form small edifices of some hundred meters in height and apparently were comparatively short-lived, such as the volcanoes in the "Tenores" field of the Canary Basin (on the order of 100 to 200 ka; Medialdea et al., 2017) and some seamounts SW of the Canary Islands (Palomino et al., 2016). Other seamounts in this region are substantially larger with complex morphologies due to multiple eruptive phases, formation of rift zones, and/or slide scars, such as Drago and Ico seamounts (Palomino et al., 2016), or Le Gouic seamount that may have formed during a period on

* Corresponding author.
E-mail addresses: akluegel@uni-bremen.de (A. Klügel), fhauff@geomar.de (F. Hauff), christoph.beier@helsinki.fi (C. Beier), Joerg.Pfaender@geo.tu-freiberg.de (J.A. Pfänder), afreundt@geomar.de (A. Freundt), mroemer@marum.de (M. Römer).

https://doi.org/10.1016/j.margeo.2024.107301
Received 7 March 2024; Received in revised form 29 April 2024; Accepted 1 May 2024
Available online 7 May 2024

the order of 1 Ma (Klügel et al., 2021) (Fig. 1a). Some of the largest seamounts such as Tropic and Echo are guyots that likely were volcanic islands before they became eroded and submerged (Schmincke and Graf, 2000; Palomino et al., 2016).

Petrological studies from the Hawaiian island chain show that large intraplate volcanoes can experience four sequential evolutionary stages as the lithosphere passes over the underlying mantle hot spot (Clague and Dalrymple, 1987). During the pre-shield, shield, and post-shield stages, the volcanic edifice is formed, and a rejuvenated or post-erosional stage may follow a hiatus in volcanic activity of up to several million years. Rejuvenated volcanism is characterized by very small volumes of silica-undersaturated alkalic lavas, indicating small degrees of mantle melting long after the volcano has passed over the hot spot (Clague, 1987). Not all large volcanoes pass through these four stages, however. For example, at the Louisville Seamount chain in the Pacific only one volcano with a rejuvenated stage has been identified thus far (Beier et al., 2011; Dorais and Buchs, 2019). In the eastern central Atlantic, where hotspot tracks are less regular than in the Pacific, rejuvenated or post-erosional stages after million year-long hiatuses were identified e.g. at Selvagem Grande island (Geldmacher et al., 2001) and the three easternmost Canary Islands (Carracedo, 1999).

Depending on the respective geotectonic situation and nature of melting anomalies, different causes for rejuvenated volcanism are possible. These include a second melting zone caused by plume flow

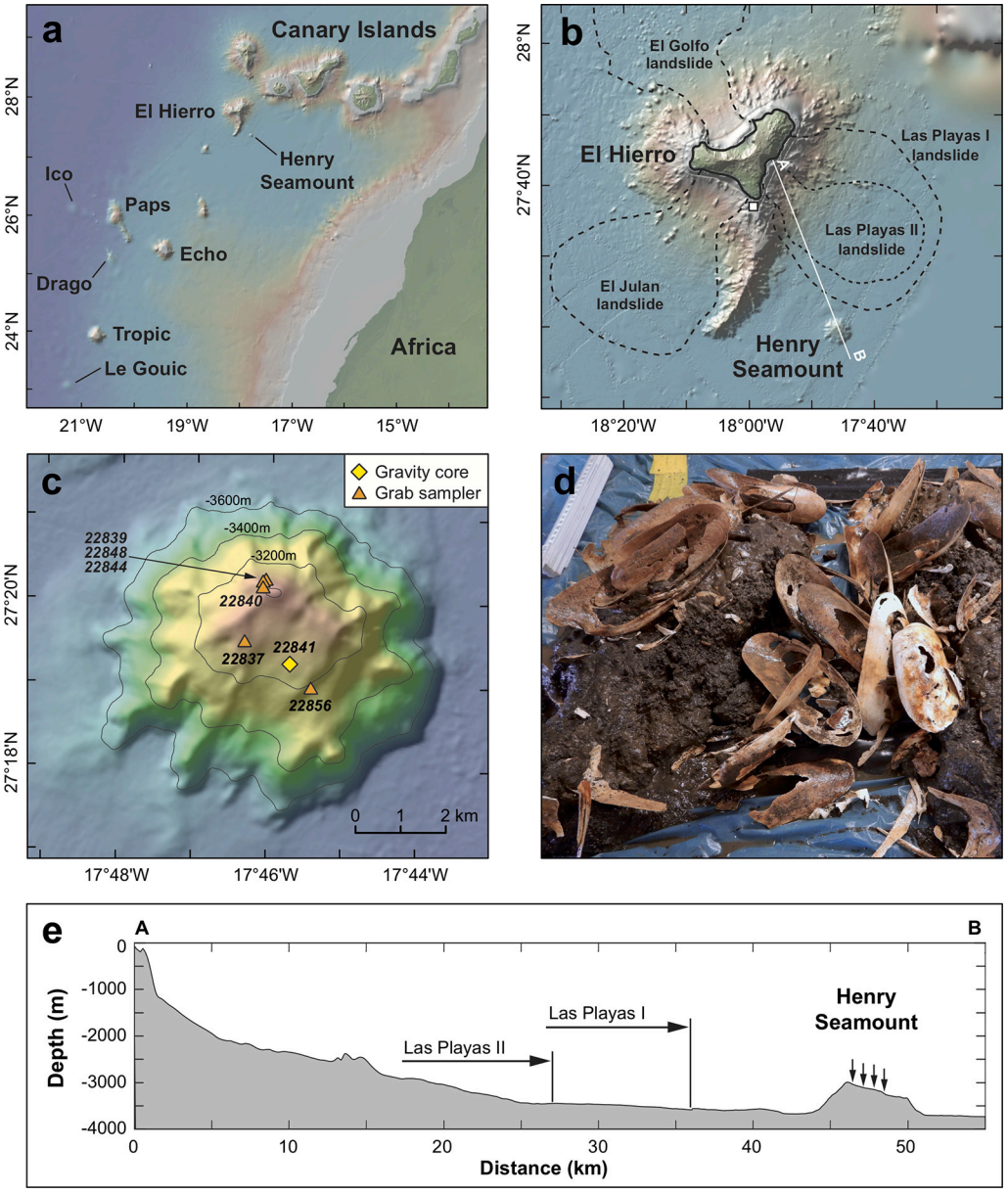

Fig. 1. (a) Overview map of the Canary Islands and the Western Sahara Seamount Province; seamount names after Palomino et al. (2016) and van den Bogaard (2013). Maps a) and b) produced using GeoMapApp (Ryan et al., 2009), with bathymetry based on GEBCO 2014. (b) Location map of El Hierro and Henry Seamount. Dashed lines outline the boundaries of landslide deposits from El Hierro after Masson et al. (2002): El Julan (>200 ka), Las Playas I (>176 ka), Las Playas II (between 145 and 176 ka), and El Golfo (between 87 and 15 ka; cf. Longpré et al., 2011). White solid line indicates profile A-B shown in panel e), white square shows locality of the 2011–2012 submarine eruption. (c) Bathymetric map of Henry Seamount with 200 m contours, showing the sites where volcaniclastic samples were recovered during cruise M146. Sample numbers are indicated in italics. (d) Photograph of grab sample 28844 with ash-rich sediment, basaltic fragments, and shell fragments from vesicomyid clams. (e) Bathymetric profile A-B from the Las Playas collapse scar to Henry Seamount (3× vertical exaggeration). Horizontal arrows indicate the extent of the Las Playas I and II landslide deposits after Gee et al. (2001a), small vertical arrows denote sample sites (cf. panel c). Note that the Las Playas II landslide reached closer to Henry Seamount than is apparent from this profile (cf. panel b).

dynamics (Ribe and Christensen, 1999); change from subsidence to uplift as a volcano overrides a flexure of the loaded lithosphere (Clague, 1987); a pulsating or blob-like mantle plume (Hoernle and Schmincke, 1993; Geldmacher et al., 2005); and metasomatic enrichment of depleted mantle that later undergoes downstream partial melting (Clague, 1987). A rejuvenated volcanic stage may also exist for solitary intraplate volcanoes not situated on a pronounced hotspot track. For example, morphologically young volcanic cones atop the flat plateau of Echo Seamount SW of El Hierro island (Palomino et al., 2016) suggest a post-erosional stage, but the length of the hiatus and cause for renewed volcanism are unknown. Plate-bound shallow mantle convection off the NW African continental margin is a viable mechanism to potentially explain both the origin of solitary seamounts and a rejuvenation of volcanic activity (van den Bogaard, 2013). Here, we report on a particular case of rejuvenated volcanic activity of Cretaceous Henry Seamount near El Hierro (Canary Islands) after a hiatus of >120 million years. Evidence for young activity is based on petrological and geochemical analyses of glassy basaltic ash recovered from the seamount summit region.

We also show that this basaltic ash is mixed with volcaniclastic fragments that likely originated from subaerial and/or submarine deposits from El Hierro. We argue that these fragments were transported by turbidity currents related to a catastrophic debris avalanche, which implies a runup of ~700 m to the top of Henry Seamount. Although it is known that such currents can surmount bathymetric barriers up to >1000 m high (e.g., Muck and Underwood, 1990), the occurrence of such deposits on top of a deep-sea seamount is a rare finding (e.g., Völker et al., 2008).

2. Regional setting

The Canary Islands are part of an intraplate hotspot chain offshore NW-Africa (Fig. 1a), with decreasing seamount and volcanic island ages from east to west. El Hierro, situated on ~155 Ma old ocean crust, is the youngest island along the chain (1.1 Ma; Guillou et al., 1996) and is located near the present Canary hotspot (Geldmacher et al., 2005). It is currently in the shield-building stage (Carracedo, 1999), with at least fifteen eruptions during the Holocene (Risica et al., 2022). The only well-documented historic eruption of El Hierro was submarine and occurred from October 2011 to March 2012 a few kilometers off the island's southern tip (e.g., Martí et al., 2013). The new volcanic cone rises to about 89 m below sea level (Rivera et al., 2013) and shows evidence for waning hydrothermal activity by the expulsion of fluids rich in magmatic CO_2 (Santana-Casiano et al., 2016). El Hierro's morphology is characterized by three large embayments that were produced by giant landslides (Hausen, 1972; Holcomb and Searle, 1991; Masson, 1996; Day et al., 1997; Urgeles et al., 1997) (Fig. 1b). On the basis of hydroacoustic data, deposits and ages of four major landslide events were identified: El Julan (>200 ka), San Andres (>176 ka), Las Playas (between 145 and 176 ka), and El Golfo, the youngest landslide on the archipelago (Gee et al., 2001a; Krastel et al., 2001; Fig. 1b). Based on onshore data the age of the El Golfo landslide is bracketed to 39–87 ka (Longpré et al., 2011) and older than 24–83 ka (León et al., 2017).

Henry Seamount, located 40 km southeast of El Hierro, is a ~ 700 m tall volcanic edifice that rises from the ~3700 m deep seafloor (Fig. 1c). It is dome-shaped with radiating gullies and ridges, largely covered by sediment, and shows a sharp break of slope with the surrounding flat seafloor (Gee et al., 2001b). A reconnaissance dredging campaign to the seamount during R/V *Meteor* cruise M66/1 yielded barite-metasomatized trachytic rocks with a $^{40}Ar/^{39}Ar$ age of 126 Ma, authigenic barite, and shell fragments from vesicomyid clams of genus *Abyssogena southwardae* (Klügel et al., 2011). It was suggested that recent hydrothermal fluid discharge had occurred at this Cretaceous seamount. In order to discover and sample potential fluid venting sites, the seamount was explored in detail during R/V *Meteor* cruise M146 by high-resolution reflection seismics, heat flow determinations, high-resolution hydroacoustic mapping, TV-sled surveys, and sediment sampling with gravity corer and Van Veen grab (Klügel and Shipboard Scientific Party, 2018). Six grab samples and one gravity core from the Henry Seamount summit area (Fig. 1c) recovered volcaniclastic sand and volcanic rock fragments up to 4 cm in size, mostly basaltic in composition. A first sample characterization is given in Klügel et al. (2020), who suggested that heat pulses from weak rejuvenated volcanic activity were, and still are, main drivers for hydrothermal circulation at Henry Seamount. In this contribution, we provide a more detailed account of the volcanic samples, including ages, trace element and short- and long-lived radiogenic isotope data.

3. Materials and methods

3.1. Sample preparation for isotope analyses and Ar—Ar dating

Fresh glassy ash fragments 0.5–3 mm in size were handpicked under a binocular and cleaned in an ultrasonic bath with deionized water three times. Rock fragments were cut with a diamond saw, local alteration rinds were removed with a small milling machine, and the cleaned material was carefully crushed to <4 mm chips. Sample splits for Ar—Ar dating were sieved to 0.25–0.5 mm. The rock chips were cleaned in an ultrasonic bath with deionized water at least three times, dried, and visually inspected under a stereo microscope to remove any alteration products. The subsequent sample preparation and cleaning steps differed between the analytical methods, see below.

3.2. Electron probe microanalysis (EPMA)

Compositions of glasses from volcaniclastics were determined on thin sections by EPMA using a Cameca SX-100 at the Faculty of Geosciences, University of Bremen. Glass was analyzed for major elements, S and Cl with an acceleration voltage of 15 kV, beam current of 40 nA, and a defocussed beam of 15 μm diameter. Peak counting times were 60 s for S and Cl and 10 s for most other elements; background counting times were half as long. Sodium was the first element to be analyzed, and a recording of intensities over time on various basalt glasses showed that no Na loss occurred during the analyses. Minerals and glasses from the Smithsonian Institution (Jarosewich et al., 1980) were used for calibration. Sulfur was calibrated using pyrite, because peak analyses indicated a predominance of S^{2-} speciation in basaltic glass samples and standards. Between two and ten EMP analyses were averaged for each glass sample. Analytical quality was monitored by repeated analyses of the glass standards VG-2 and VG-A99 (Smithsonian) and BHVO-2G and BCR-2G (USGS; Jochum et al., 2005) along with the samples (Table S1). Precision of S analyses was 3.5% for VG-2 (1400 μg/g), and 18% for VG-A99 (150 μg/g).

3.3. Laser ablation inductively coupled plasma mass spectrometry (LA-ICP-MS)

LA-ICP-MS analyses were carried out on thin sections, using a NewWave UP193ss laser coupled to a Thermo Element2 at the Faculty of Geosciences, University of Bremen. Major element analyses of groundmass followed the protocol described in Klügel et al. (2022). Trace element analyses used a laser beam between 25 and 75 μm diameter for glass and 100 μm for groundmass, with 5 Hz pulse rate. Glasses were analyzed on-spot with a dwell time of 60 s, whereas groundmass was analyzed along a raster at 5 μm/s for 240 s to give a single analysis. Between three and six single analyses were averaged. All isotopes were analyzed at low resolution with five samples in a 20% mass window and a total dwell time of 25 ms per isotope. As oxide formation was low (ThO/Th ≤ 0.1%), no mass interference corrections were applied. Trace element analyses were quantified using the Cetac GeoPro™ software with standard reference material (SRM) NIST610 glass for external calibration and Ca as internal standard element. Analytical precision

and accuracy were monitored by regular analyses of USGS basalt glasses BHVO-2G and BCR-2G (Jochum et al., 2005) along with the samples; both were better than 5% for most elements (Table S2).

3.4. Sr-Nd-Pb isotope analyses

Strontium, Nd and Pb ion chromatography and mass spectrometry followed procedures outlined in Hauff et al. (2021). In summary about 100 mg of rock chips were leached in 2 N HCl for 1 h at 70 °C followed by triple rinsing in 18 MΩ H_2O and dissolution in closed Teflon beakers using a 5:1 mixture of concentrated HF-HNO_3 at 130 °C over 48 h. Lead double-spike mass-bias corrected values of SRM NBS981 on the Thermo Triton® Plus TIMS are $^{206}Pb/^{204}Pb = 16.9408 \pm 0.0018$, $^{207}Pb/^{204}Pb = 15.4974 \pm 0.0019$, $^{208}Pb/^{204}Pb = 36.7205 \pm 0.0048$, $^{207}Pb/^{206}Pb = 0.914799 \pm 0.000048$, and $^{208}Pb/^{206}Pb = 2.167580 \pm 0.000095$ ($n = 266$, 2 standard deviations (SD)) since installation of the instrument in 2014. Strontium and Nd isotope ratio measurements on the Triton Plus TIMS were mass-bias corrected within run to $^{86}Sr/^{88}Sr = 0.1194$ and $^{146}Nd/^{144}Nd = 0.7219$, respectively. SRM NBS987 (Sr) and La Jolla (Nd) measured along with the samples gave $^{87}Sr/^{86}Sr = 0.710250 \pm 0.000008$ ($n = 31$, 2 SD) and $^{143}Nd/^{144}Nd = 0.511850 \pm 0.000006$ ($n = 28$, 2 SD). The long-term reproducibility of radiogenic Sr-Nd-Pb isotope ratios on leached BCR-2 international rock standard at GEOMAR can be found at https://www.geomar.de/en/research/fb4/fb4-muhs/infrastructure/tims. Typical procedural blanks for Sr-Nd-Pb are <100 pg, <50 pg and < 30 pg respectively.

3.5. Uranium-series isotope analyses

Uranium-series were analyzed on fresh, hand-picked unaltered volcanic glass samples which were washed, leached, and manually re-inspected twice prior to the addition of spikes, dissolution, and column chemistry as described in Beier et al. (2010) and Turner et al. (2011). The samples were analyzed at the Wollongong Isotope Geochronology Laboratory, University of Wollongong, Australia. The U and Th cuts were analyzed on a ThermoFisher Neptune® MC-ICP-MS following the method described in Dosseto et al. (2006) and Francke et al. (2018). For U analyses, the New Brunswick Laboratory (NBL) synthetic standards U010 and U005a were analyzed at regular intervals. For Th analyses, a standard-sample bracketing procedure was used for each sample, bracketing with the Th 'U' standard solution and values checked independently with the Th 'A' solution; a linear tail correction for the ^{232}Th tail on ^{230}Th was applied (Sims et al., 2008). The accuracy was better than 3.8% determined by repeated analysis of the BCR-2 international rock standard that was processed along with the other samples throughout the whole analysis. The Ra cuts were analyzed with a ThermoFinnigan Triton® TIMS at Macquarie GeoAnalytical facility (MQGA) at Macquarie University, Sydney, Australia, after being loaded onto degassed Re filaments with a Ta-HF–H_3PO_4 solution. The accuracy of BCR-2 standard analysis is 0.53% for ^{226}Ra and 1.33% for ($^{226}Ra/^{230}Th$) (Scott et al., 2019; Sims et al., 2013). Typical blanks for U and Th are 100 and 50 pg, respectively, which is negligible compared to the amounts in the samples.

3.6. Ar—Ar dating

Due to a lack of K-bearing minerals, crushed and handpicked whole rock fragments (0.25–0.5 mm sieve fraction) from samples 22844-1A, 22844-1E and 22848-1A were selected for age dating by the ^{39}Ar—^{40}Ar method. The sample splits were leached for 5 min in ~5% nitric acid in an ultrasonic bath to remove any carbonate, then they were repeatedly ultrasonicated in deionized water. After drying, the splits were wrapped in *Al* foil and loaded along with fluence monitors in wells of an *Al* disc (33 mm diameter). Irradiation was done for 18 h at a reactor power of 8.2 MW (samples 22844-1A, 22844-1E) respectively 25 h at 9.6 MW (sample 22848-1A) in the rotational channel of the LVR-15 research reactor of the Research Centre in Řež (CVŘ), Czech Republic. The thermal neutron flux was $\sim 3.7 \times 10^{13}$ n cm^{-2} s^{-1} at a reactor power of about 8.2 MW and a thermal to fast neutron ratio of ~5.

After irradiation, the sample splits were loaded either into small Mo-crucibles for furnace step heating (up to 250 mg per sample), or in 7 or 9 mm cylindrical counterbores, 2 mm in depth, on a copper disc for thermal laser step heating (up to 30 mg per sample). The furnace used was a Createc high-temperature cell (HTC; for details see Pfänder et al., 2014), the thermal laser system was a 25 W Synrad CO_2-laser operated in continuous mode and coupled to a Raylase Scanhead for beam deflection. Deflection frequencies were 15 and 290 Hz on the x and y axes, and the amplitude of the Scanhead was set correspondingly to cover the individual sizes of a counterbore. Gas purification was achieved by two SAES GP50 getter pumps, one at room temperature and one at 400 °C. Heating and cleaning times were 10 min each per step for the HTC, and 5 min each for laser step heating.

Argon isotope compositions during furnace step heating were measured in static mode on a GV Instruments ARGUS noble gas mass spectrometer equipped with five faraday cups and 10^{12} Ω resistors for ^{36}Ar to ^{39}Ar and a 10^{11} Ω resistor for ^{40}Ar. Typical blank levels are 2.5×10^{-16} mol ^{40}Ar and 8.1×10^{-18} mol ^{36}Ar. Measurement time was 7.5 min per temperature step acquiring 45 scans at 10 s integration time each. For the laser heating experiments, Ar isotope compositions were measured in multi-dynamic mode on a Thermo ARGUS VI noble gas mass spectrometer equipped with five faraday cups (10^{11} Ω resistor at position H2, 10^{12} Ω resistors at positions H1 to L2) and a CDD multiplier at the low mass side (L3). Intercalibration of the CDD was done externally during airshot measurements and relatively to the L2 Faraday cup using a beam current of 25–40 fA on mass 36. Typical blank levels range between 0.5×10^{-16} to 1.4×10^{-16} mol ^{40}Ar and 1.0×10^{-18} to 3.4×10^{-18} mol ^{36}Ar. Twenty cycles with a total duration of ~9 min were measured per temperature step. Each cycle comprised two aquisition sequences with masses 38 and 39 on the axial cup, respectively, and 8.4 s integration time plus 5.0 s delay time per sequence. Mass bias was corrected assuming linear mass dependent fractionation and using an atmospheric $^{40}Ar/^{36}Ar$ ratio of 298.6 ± 0.3 (Lee et al., 2006). For raw data reduction and time-zero intercept calculation an in-house developed Matlab® toolbox was used; isochron, inverse isochron and plateau ages were calculated using ISOPLOT 3.7 (Ludwig, 2008). All ages were calculated relative to the in-house standard DRF1 (Drachenfels sanidine) as a fluence monitor with an age of 25.682 ± 0.030 Ma, calibrated against a Fish Canyon Tuff sanidine age of 28.305 ± 0.036 Ma (Renne et al., 2010). All reported errors are 1 SD.

4. Results

4.1. Occurrence and petrography of volcaniclastic rock samples

The volcanic rock samples recovered from grabs and gravity cores during M146 comprise volcaniclastic-dominated layers as well as dispersed particles and clasts (Klügel et al., 2020) (Table 1). In the following descriptions and discussion, we divide the samples according to the dominant grain size into volcaniclastic ash that can also contain granules and minor particles up to 10 mm diameter, and volcaniclastic lapilli (gravel) here typically 0.5–4 cm in size, irrespective of their origin.

4.1.1. Volcaniclastic ash

Heterolithologic, poorly to moderately sorted basaltic ash layers, at least several cm thick, were sampled in the summit area of Henry Seamount by grabs 22840 and 22844 and by gravity core 22841 (Fig. 1c, 2b). In none of the samples could a stratification or gradation be recognized, but neither the gravity core nor the grabs penetrated through the entire volcaniclastic layer. These ash layers contain a minor fraction of bioclasts typically <1 mm in size, and dispersed volcanic rock fragments up to 3 cm in size (see below). Grabs 22840 and 22844 also

Table 1
Localities and lithologies of investigated samples.

Sample#	IGSN	Longitude	Latitude	Depth	Sampling	Sample type	Matrix	Macrocrysts (>0.1 mm)
		[degrees E]	[degrees N]	[m bsl]				
22837-1A	IEKLA0005	−17.7722	27.3251	3082	Grab	Basalt fragment, vesicular	Groundmass, vesicular	none
22839-1A	IEKLA0006	−17.7675	27.3374	3060	Grab	Basalt fragment, glassy	Glassy	Ol, Cpx, Mt
22839-1B	IEKLA0007	−17.7675	27.3374	3060	Grab	Basalt fragment	Groundmass	Ol, Plag, few Cpx and Mt
22839-1C	IEKLA0008	−17.7675	27.3374	3060	Grab	Dolerite fragment	Coarse groundmass	Plag, Cpx, Ol, Mt
22840-1A	IEKLA0002	−17.7680	27.3363	3025	Grab	Tephra (ash to lapilli)	Mixed lithology	mixed lithology
22841-1A	IEKLA0001	−17.7620	27.3216	3145	GC, 36–38 cm	Tephra (ash to lapilli)	Mixed lithology	mixed lithology
22844-1A	IEKLA0009	−17.7679	27.3371	3061	Grab	Phonotephrite fragment	Glassy, vesicular	Plag, Mt., few Cpx
22844-1B	IEKLA0010	−17.7679	27.3371	3061	Grab	Basalt fragment	Groundmass	Cpx, Ol, few Mt. and Plag
22844-1C	IEKLA0011	−17.7679	27.3371	3061	Grab	Basalt fragment	Glassy	Ol, Cpx, Plag
22844-1D	IEKLA0012	−17.7679	27.3371	3061	Grab	Trachyte fragment	Groundmass	Fsp, Amph, Cpx, Mt
22844-1E	IEKLA0013	−17.7679	27.3371	3061	Grab	Basalt fragment	Groundmass	Plag, few Cpx
22844-1F	IEKLA0014	−17.7679	27.3371	3061	Grab	Basalt fragment	Groundmass	Cpx, Plag
22844-1G	IEKLA0015	−17.7679	27.3371	3061	Grab	Basalt fragment	Groundmass, partly glassy	Ol, Plag, Mt
22844-1H	IEKLA0016	−17.7679	27.3371	3061	Grab	Basalt fragment	Groundmass, partly glassy	Plag, few Amph
22844-1I	IEKLA0017	−17.7679	27.3371	3061	Grab	Basalt fragment	Groundmass, altered	Ol, Cpx, Plag, Mt
22844-1L	IEKLA0003	−17.7679	27.3371	3061	Grab	Tephra (ash to lapilli)	Mixed lithology	mixed lithology
22848-1A	IEKLA0019	−17.7676	27.3372	3042	Grab	Basalt fragment	Groundmass, partly glassy	Ol, Mt., Plag, Cpx
22848-1B	IEKLA0020	−17.7676	27.3372	3042	Grab	Dolerite fragment	Coarse groundmass	Plag, Cpx, Ol, Mt
22848-1C	IEKLA0021	−17.7676	27.3372	3042	Grab	Basalt fragment	Groundmass	Plag, few Cpx
22848-1E	IEKLA0004	−17.7676	27.3372	3042	Grab	Tephra (ash to lapilli)	Mixed lithology	mixed lithology
22856-1A	IEKLA0025	−17.7571	27.3160	3241	Grab	Basalt fragment	Groundmass, partly glassy	Plag, few Ol

Abbreviations: IGSN, International Geosample Number; GC, gravity core; bsl: below sea level;
Ol: olivine; Cpx: clinopyroxene; Plag: plagioclase; Fsp: feldspar; Amph: amphibole; Mt: magnetite.
For the full sample number the prefix "GeoB" has to be added, e.g., GeoB 22837-1A.

contained shells and shell fragments from vesicomyid clams (Fig. 1d). In both grab samples the volcaniclastics were the dominating part, overlain by a thin layer of brownish calcareous ooze and partly mixed with it (Fig. 1d). During their recovery a smell of H_2S was discernible for some minutes. In grab 22840 the ash was locally cemented by barite, forming platy tuffaceous aggregates. No distinct ash layer was recovered by grab 22848, which only contained ash particles dispersed in foraminifer-rich calcareous ooze and in cemented sediment pieces. In gravity core 22841, the upper 3–4 cm of an ash layer were retrieved, overlain by ~13 cm of brownish pelagic sediment (Fig. 2c). The ash is lithologically similar to that in the grab samples (Fig. 2d). Since sediment penetration by gravity core and heat probe during cruise M146 failed in most cases, we infer that the ash layer is widespread in the summit area of Henry Seamount and has considerable thickness in some places. The lack of similar volcaniclastic layers in the other eleven grab samples from the seamount (Klügel and Shipboard Scientific Party, 2018) suggests that the thickness of the sediment cover varies greatly, probably as a result of local bottom currents.

The lithology of the volcaniclastic ash is very diverse. Vesicular sideromelane particles with olivine macrocrysts ± plagioclase ± rare clinopyroxene microlites are predominant (Fig. 2d) and are denoted as ash type A. These particles have about 20–50% vesicularity with most vesicles <0.5 mm in size and comparatively thick bubble walls. The moderately vesicular particles are typically angular and blocky, but the shape of some more vesicular particles is dominated by broken vesicles. Flat bubble wall fragments similar to Limu o Pele were not observed. Although most particles are <4 mm in size, some reach 10 mm. Olivine macrocrysts (composition $Fo_{80–83}$) are euhedral to subhedral, <2 mm in size, and occur isolated or in clusters (Kahl et al., 2022). Many olivines show planar aggregates of pyrite ± marcasite within cavities inside the crystals. The cavities occur along cracks and/or form negative crystal shapes within the olivines or in the host glass. Kahl et al. (2022) suggested that this olivine dissolution and FeS_2 precipitation was caused by H_2S-bearing fluids that infiltrated the ash layer. Apart from that, ash type A particles are fresh and show no palagonitization. Overall, the morphology of ash type A particles closely resembles pyroclasts from deep-sea strombolian eruptions of volatile-rich magma (Clague et al., 2003; Eissen et al., 2003; Davis and Clague, 2006).

In addition to the predominant ash type A, the ash fraction includes the following lithologies: 1) sideromelane matrix with clinopyroxene (Cpx) ± olivine (Ol) ± Fe-Ti oxide (Mt) macrocrysts; 2) sideromelane matrix with abundant plagioclase (Plag) laths and flow texture; 3) sideromelane matrix with Cpx microlites and Cpx + Ol macrocrysts; 4) basaltic groundmass with Plag macrocrysts; 5) basaltic groundmass with Cpx macrocrysts; and 6) single Ol or Cpx crystals. Some of the glassy fragments show incipient alteration on rims or cracks, and most of the particles are vesicular. There are also a number of variably altered particles of different lithologies that were not further investigated.

4.1.2. Volcaniclastic lapilli

Fragments of igneous rocks up to 4 cm in size were retrieved from six grab samples and from the core catcher of gravity core 22841 (Table 1). In grab samples 22837, 22839, 22848 and 22856 the fragments were dispersed in brownish calcareous ooze, and in the others within the volcaniclastic ash layer (Fig. 1d). Most fragments are angular to edge-rounded with irregular surfaces (Fig. 2a). The color is predominantly gray to black, with brownish to orange surfaces where incipient alteration had occurred. A few samples are highly vesicular, but most are dense and contain few if any vesicles (Fig. 2e). The low vesicularity of most lapilli samples is a major difference to the ash layers described above. In the size range between 0.5 and 1 cm, however, there is an increasing proportion of vesicular and partly glassy fragments of possible pyroclastic origin. Most of the larger fragments appear to derive from lava flows, as is indicated, for example, in sample 22844-1H by flow-aligned plagioclase crystals (Fig. 2e). Predominantly spherical to elliptical vesicle shapes in glassy lava (e.g., sample 22844-1A in Fig. 2e) indicates little shear during rapid quenching.

Based on matrix type and phenocryst assemblages various lithologies can be distinguished (Fig. 2e), including: 1) basalt with Ol + Cpx ± Plag macrocrysts set in a microcrystalline groundmass; 2) basalt with Ol + Cpx ± Plag in a glassy matrix; 3) basalt to intermediate rock with aligned Plag laths; 4) fine-grained basalt with Plag laths and few other macrocrysts; 5) aphyric vesicular basalt; 6) fresh vesicular phonotephrite glass with plagioclase laths; 7) dolerite-like rock with Ol macrocrysts in a coarse-grained matrix of Plag + Cpx + Mt; 8) trachytic rock with Plag + kaersutitic amphibole + apatite macrocrysts in a groundmass of anorthoclase with minor amounts of apatite. The trachytic rock is considerably altered and is likely a fragment of the Henry Seamount

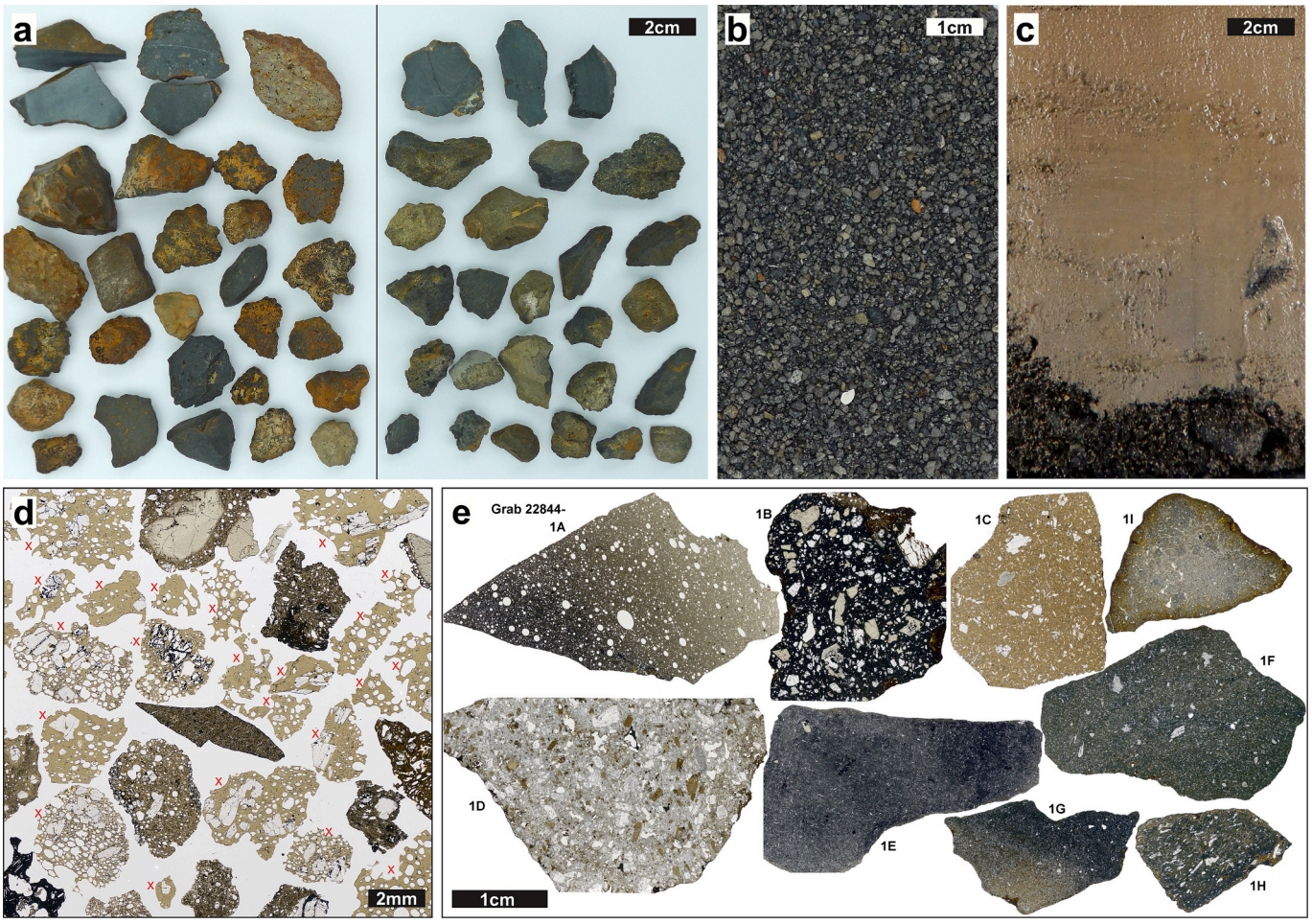

Fig. 2. Photographs (a, b, c) and microphotographs (d, e) of samples from Henry Seamount. (a) Volcaniclastic lapilli recovered from grab samples 22844 (left) and 22848 (right). Note the angularity of many fragments, the various lithologies, and the variably weathered clast surfaces. (b) Volcaniclastic ash from grab sample 22840 (0.5–2 mm sieve fraction), consisting of predominant type A ash and other heterolithologic clasts. (c) Bottom of gravity core (sample 22841-1A) showing an ash layer overlain by pelagic sediment. (d) Microphotograph of thin section from the ash (>0.5 mm fraction) shown in panel c) reveals a variety of lithologies. Glassy olivine-phyric type A ash particles are marked by red crosses. (e) Microphotographs of complete thin sections of nine volcaniclastic lapilli from grab 22844 illustrate considerable lithological varieties. Sample numbers are indicated and correspond to those in Table 1. The spherical to elliptical shape of most vesicles in the fresh glassy phonotephrite (sample 22844-1A) indicates little shear during rapid quenching, as is typical of a submarine lava. Note the paucity of vesicles in all other samples, the flow alignment of plagioclase crystals in sample 22844-1H, and the alteration rind with local palagonite (orange color) in sample 22844-1I. Sample 22844-1D is an evolved rock (trachyte). (For interpretation of the references to color in this figure legend, the reader is referred to the web version of this article.)

basement (cf. Klügel et al., 2011).

4.2. Major and trace element composition

We analyzed glasses and microcrystalline groundmass from various volcaniclastic samples from Henry Seamount; all analyses are presented in Table S3. Based on their chemical composition, the samples can be subdivided into two groups (Fig. 3a,b). Group 1 are transitional to alkalic basalts with a limited compositional range of 43.5–46.5 wt% SiO_2, 6.1–7.4 wt% MgO, 3.2–4.3 wt% total alkalis; comparatively high Na_2O/K_2O of 4.0–6.6, and Mg# of 43.1–50.5 (Mg# = molar Mg/(Mg + Fe^{tot})*100). This group comprises the dominant ash type A and the single dolerite fragment analyzed (sample 22839-1C). Group 2 comprises all other ash and lapilli samples, with a wide compositional range from basanite to trachybasalt to phonotephrite. The compositions of group 2 samples overlap largely with bulk rock and glass data from subaerial and submarine rocks from El Hierro island, with some exceptions for e.g. P_2O_5 and Al_2O_3. In contrast, group 1 samples strongly differ from El Hierro in being lower in alkalis and P_2O_5, and higher in CaO and Na_2O/K_2O, at given MgO or SiO_2 (Fig. 3a). Group 1 samples are also distinguished by their distinctly higher Ba/Th, Nb/U, Nb/Th, and lower Sm/Yb, La/Sm, and La/Nb ratios, at a given concentration of a highly incompatible element such as Th (Fig. 3b).

The differences between group 1 and 2 samples are also expressed in their trace element patterns. On primitive mantle-normalized incompatible element diagrams, samples from both Henry Seamount and El Hierro show features characteristic of enriched mantle (EM) basalts (Willbold and Stracke, 2006), which includes relative enrichment of Nb and Ta and depletion of Pb (Fig. 4a). The strong depletion of the heavy relative to the middle and light rare earth elements (REE) indicates the presence of garnet in the source (Fig. 4b). The trace element patterns of group 2 samples essentially overlap with El Hierro lavas, whereas those for group 1 samples tend to have lower concentrations of the most incompatible trace elements, a small positive Ti anomaly, and flatter REE patterns.

4.3. Sulfur in glass

Sulfur was analyzed in glassy ash and lapilli samples to place constraints on the origin of the volcaniclastics and particularly on the water depth where the eruption occurred. The S content of a magma strongly depends on degassing during ascent, and hence on the pressure at which

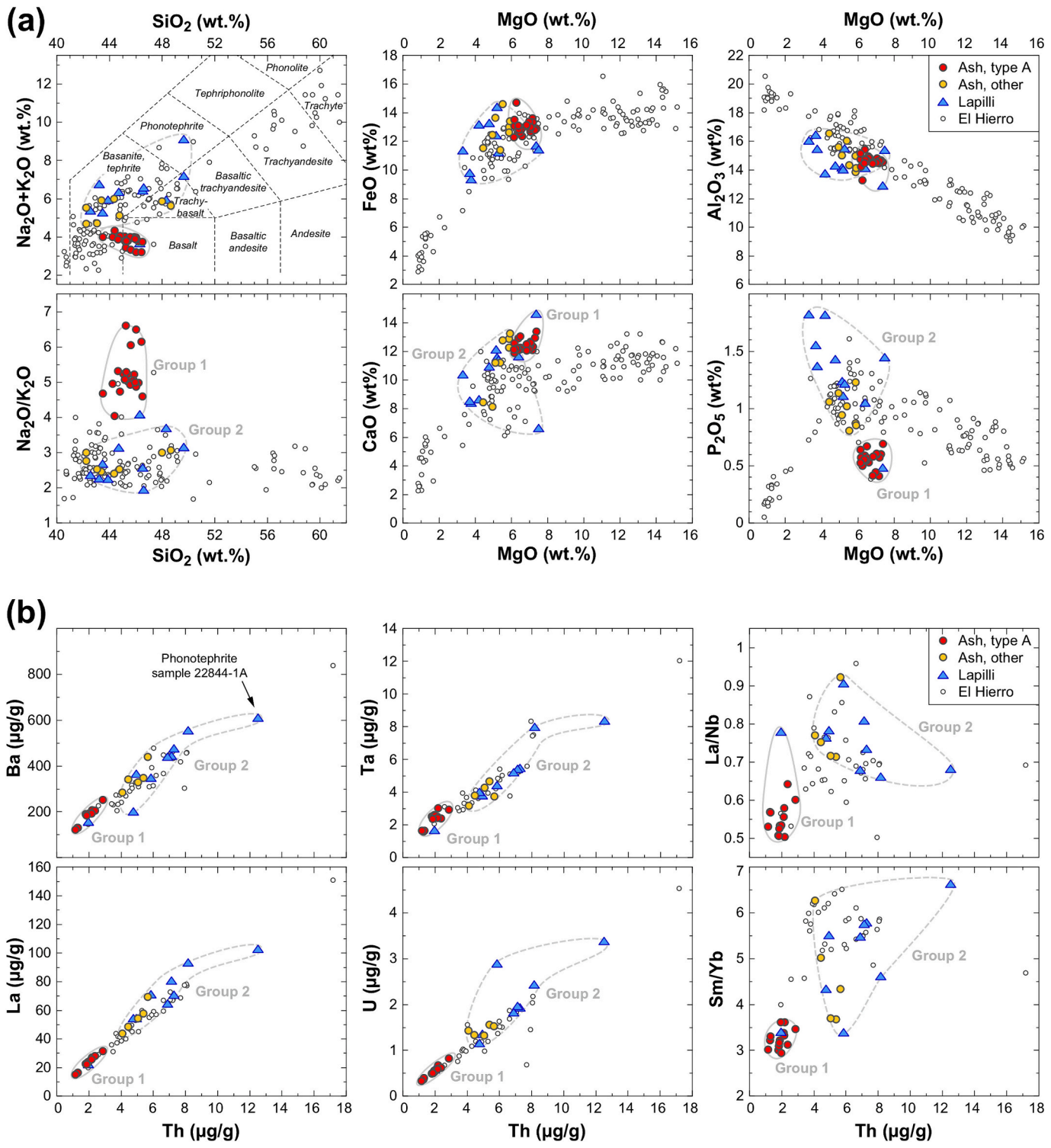

Fig. 3. Compositions of matrix glass and microcrystalline groundmass from Henry Seamount samples, including those from Klügel et al. (2020): Type A ash (red circles), other ash (yellow circles), and lapilli (blue triangles). Based on their chemical composition the data are subdivided into group 1 samples (gray solid line) and group 2 samples (gray dashed line), see text. Data for submarine and subaerially erupted El Hierro rocks are shown for comparison (small open circles). (a) Harker diagrams with all analyses normalized to 100 wt% volatile-free. Each data point for Henry Seamount is the average of between 2 and 16 single spot or raster analyses. El Hierro data include bulk-rock compositions from submarine and subaerial eruptions (Pellicer, 1979; Carracedo et al., 2001; Day et al., 2010; Klügel et al., 2011) and glasses from the 2011–2012 submarine eruption (Longpré et al., 2014). (b) Diagrams of incompatible trace elements and element ratios versus Th. El Hierro data from Day et al. (2010) and Klügel et al. (2011). (For interpretation of the references to color in this figure legend, the reader is referred to the web version of this article.)

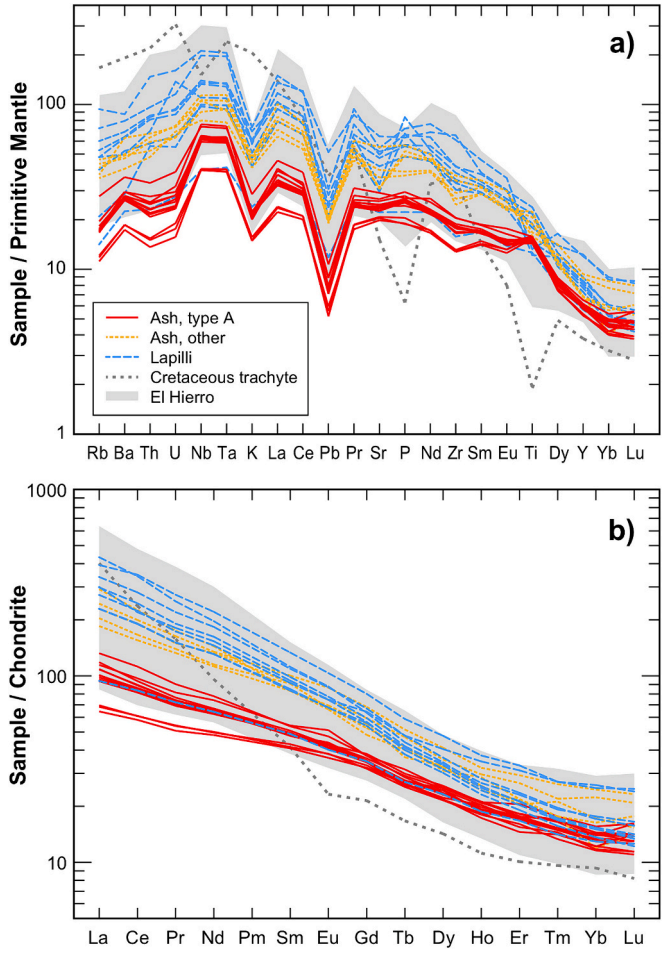

Fig. 4. (a) Primitive mantle-normalized incompatible element diagram, and (b) chondrite-normalized REE diagram, of samples from Henry Seamount and El Hierro; normalization values after Sun and McDonough (1989). Each analysis from Henry Seamount is the average of between 2 and 16 single spot or raster analyses. Type A ash samples are characterized by low concentrations of the most incompatible elements and comparatively flat REE patterns. The lapilli sample having compositions similar to type A ash is a dolerite fragment (sample 22839-1C). Data for subaerial and submarine El Hierro samples are from Day et al. (2010), Klügel et al. (2011), and Longpré et al. (2014); average Cretaceous Henry Seamount trachyte composition from Klügel et al. (2011).

the melt is quenched (Wallace and Edmonds, 2011). This is well exemplified by glasses from subaerial and submarine El Hierro samples, as they show a good correlation between S content and eruption depth (Klügel et al., 2020; Fig. 5a). Glasses from Henry Seamount have significantly higher S contents in type A ash (660–960 μg/g) than in other ash (370–710 μg/g) or lapilli samples (170–310 μg/g), but even the highest contents do not plot along the El Hierro trend, which extrapolates to >1600 μg/g at 3000 m water depth (Fig. 5a). The picture is different, however, when S/K_2O rather than S is plotted in order to eliminate bias from petrogenetic processes. Because S and K are similarly compatible in basaltic melts, the S/K_2O ratio changes little during mantle melting and crystal fractionation but decreases during degassing (Wallace and Edmonds, 2011). Type A ash samples have similar or higher S/K_2O ratios (0.10–0.20) than submarine El Hierro rocks (0.02–0.16), indicating that they are actually the least degassed samples (Fig. 5b). Other ash particles from Henry Seamount are stronger degassed with S/K_2O of 0.03–0.06, whereas the lapilli all have low S/K_2O (<0.02) similar to degassed subaerial El Hierro pyroclasts. In a plot of S/K_2O versus K_2O (Wallace and Edmonds, 2011), which separates the effects of mantle melting, crystal fractionation, and degassing, the

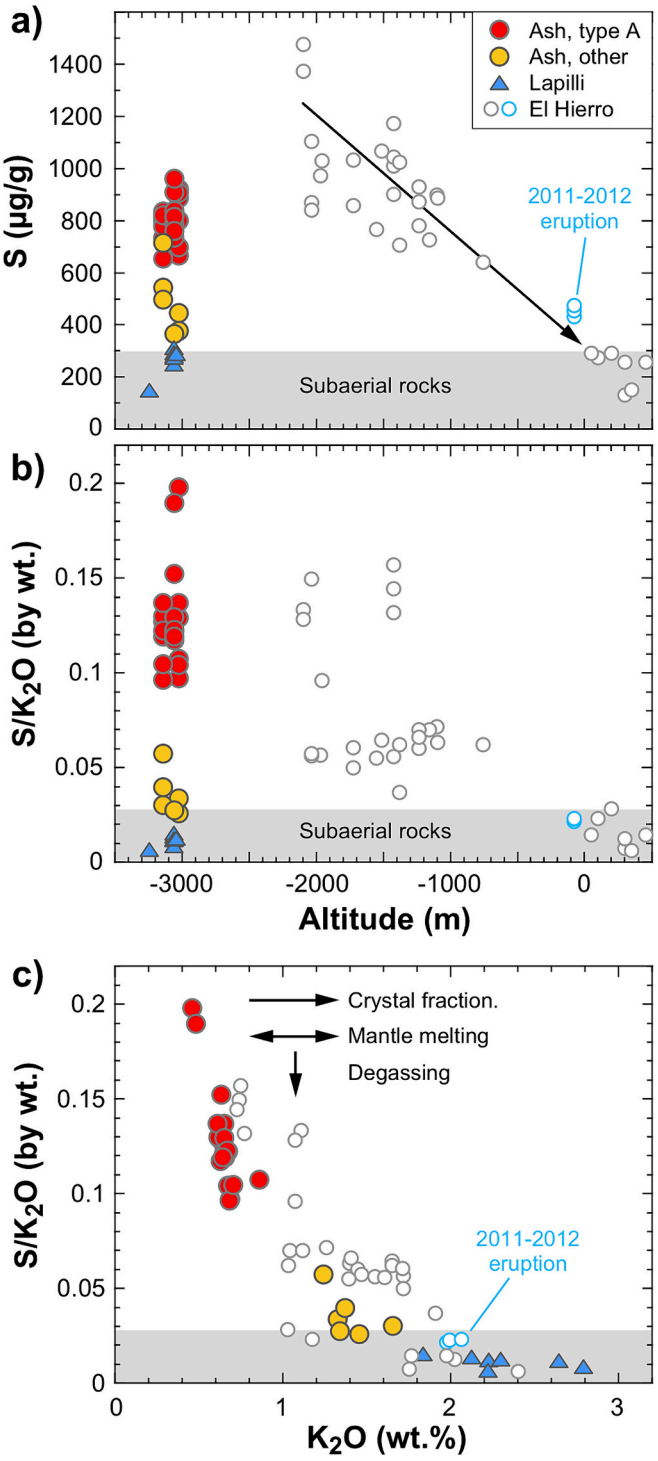

Fig. 5. (a) Sulfur contents and (b) S/K_2O ratios of matrix and interstitial glasses from Henry Seamount samples and from submarine and subaerial El Hierro rocks (Stroncik et al., 2009; Klügel et al., 2020), plotted against the altitude of the samples. The arrow highlights the good correlation between altitude and S content for the El Hierro data, indicating a strong pressure control on sulfur degassing. The Henry Seamount samples do not plot along the El Hierro trend, but have similar or even higher S/K_2O ratios, showing that type A ash includes the least degassed samples. (c) A plot of S/K_2O versus K_2O for the same data set illustrates the different effects of degassing and crystal fractionation / mantle melting (Wallace and Edmonds, 2011). In this diagram the Henry Seamount and El Hierro samples plot within a coherent array; the same relation is displayed if P_2O_5 or another incompatible element is used for the abscissa.

samples from Henry Seamount and El Hierro form a coherent data array (Fig. 5c).

4.4. Sr-Nd-Pb and U-Th-Ra isotopes

We analyzed three samples of type A ash and six lapilli (group 2 samples) from Henry Seamount for their Sr-Nd-Pb isotopic composition, and one basanite from the 2011–2012 submarine El Hierro eruption for comparison (Table S4). On the Sr—Nd isotope diagram the Henry Seamount samples show a good negative correlation, broadly coinciding with the trend defined by subaerial and submarine rocks from El Hierro and adjacent La Palma island (Fig. 6a). Their Sr—Nd isotopic character is depleted with higher $^{143}Nd/^{144}Nd$ (0.51290–0.51298) and lower $^{87}Sr/^{86}Sr$ (0.7029–0.7032) than primitive mantle (e.g., Zindler and Hart, 1986), except for type A ash sample 22840-1A ($^{87}Sr/^{86}Sr = 0.7068$). The three type A ash samples have the highest $^{87}Sr/^{86}Sr$ and include the lowest $^{143}Nd/^{144}Nd$ ratios, which may reflect mild seawater alteration as observed in some ash particles (Kahl et al., 2022), and/or contamination by deep-sea sediment that could not be removed during sample processing and leaching. On both the thorogenic and uranogenic Pb diagrams, group 2 samples plot close to the Northern Hemisphere Reference Line (NHRL) of Hart (1984), forming narrow linear arrays with correlation coefficient r^2 of 0.989 and 0.990, respectively. They also correlate negatively in Pb—Nd isotope space (Fig. 6b); the least radiogenic sample in the Pb isotope diagrams (22837-1A: $^{206}Pb/^{204}Pb = 19.19$, $^{207}Pb/^{204}Pb = 15.57$, $^{208}Pb/^{204}Pb = 38.83$) is also the isotopically most depleted sample in Sr—Nd space. Type A ash samples plot slightly above the NHRL, with a weak tendency towards the field for marine sediments south of Gran Canaria (Hoernle et al., 1991) (Fig. 6 c, d). In summary, group 2 samples from Henry Seamount are indistinguishable from El Hierro samples with respect to Sr-Nd-Pb isotopes. Type A ash samples, in contrast, show small but systematic deviations of elevated $^{207}Pb/^{204}Pb$ and $^{208}Pb/^{204}Pb$ and lower $^{143}Nd/^{144}Nd$ at a given $^{206}Pb/^{204}Pb$ from the El Hierro isotope arrays. This offset may be due to interaction with seawater and sediment or to differences in the mantle source.

In addition to Sr-Nd-Pb isotopes, we analyzed the glassy phonotephrite fragment 22844-1A and the type A ash sample 22841-1A from Henry Seamount, as well as the basanite from the 2011–2012 El Hierro eruption, for U-series disequilibria (Table S5). The range of Th and U concentrations is 2.1–15.6 and 0.6–4.1 μg/g, respectively, while ^{226}Ra concentrations vary from 1.17 to 1.76 pg/g. The activity ratio (^{238}U)/(^{232}Th) for these samples shows little variation (0.79–0.81) and is within the range of Holocene to late Pleistocene volcanic rocks from El Hierro

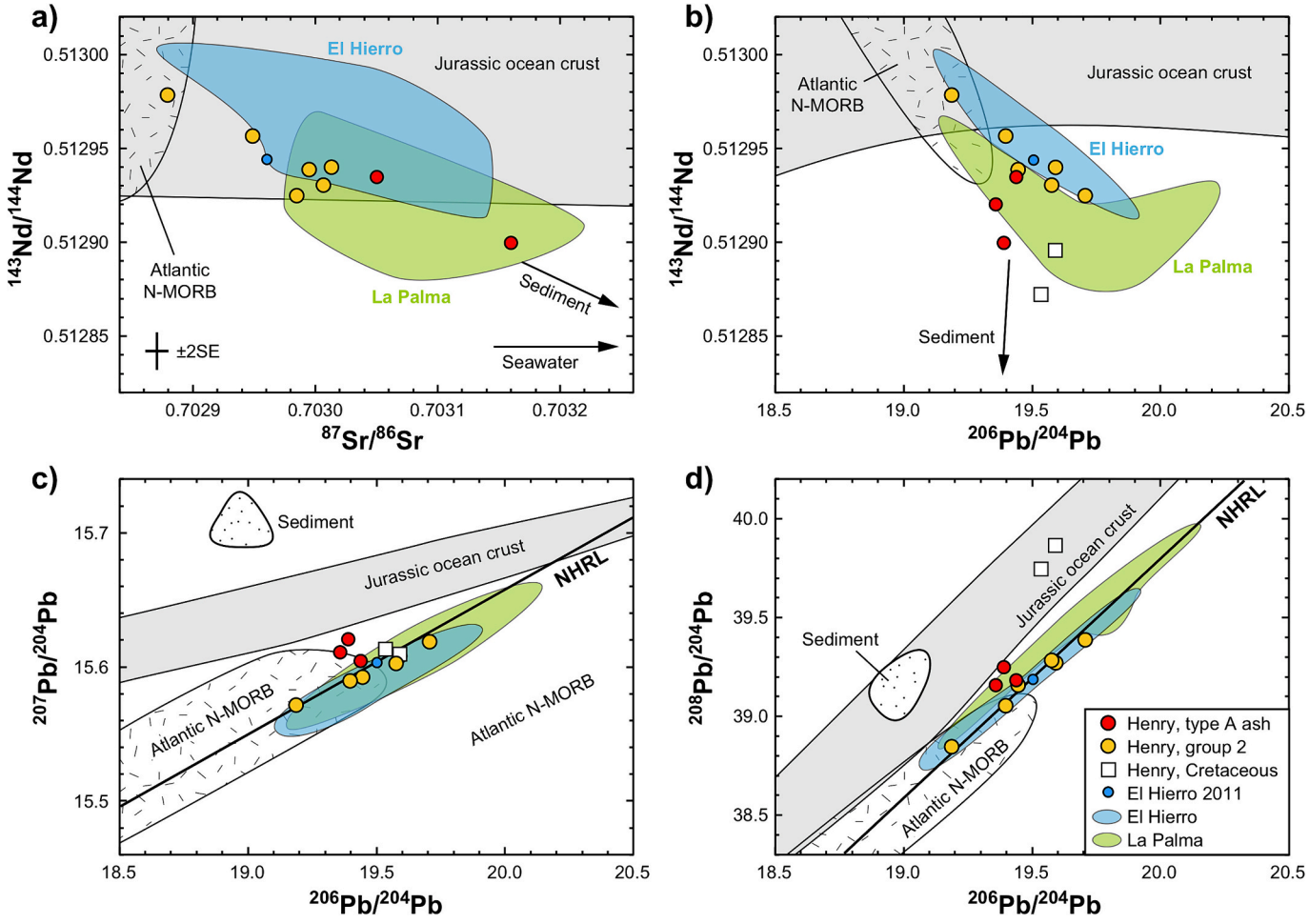

Fig. 6. Isotope correlation diagrams of samples from Henry Seamount: (a) Sr-Nd; (b) Pb-Nd; (c) thorogenic Pb diagram; (d) uranogenic Pb diagram. Note that type A ash sample 22840-1A plots off scale for $^{87}Sr/^{86}Sr$ (0.7068). The data indicate large overlap of Henry Seamount samples with subaerial and submarine rocks from the two westernmost Canary Islands of El Hierro (Abratis et al., 2002; Day et al., 2010) and La Palma (Abratis et al., 2002; Johansen et al., 2005; Gurenko et al., 2006; Day et al., 2010; Turner et al., 2015; Klügel et al., 2017). Type A ash samples show small systematic deviations from the El Hierro Nd—Pb isotope arrays, suggesting a role of a sediment component. Analytical uncertainties (+ − 2 standard errors, SE) are indicated for Sr and Nd, and are smaller than symbol sizes for Pb isotope ratios. Data for Cretaceous Henry Seamount trachytes from Klügel et al. (2011); fields for Jurassic ocean crust after Hoernle (1998), for marine sediments south of Gran Canaria after Hoernle et al. (1991), and for Atlantic N-MORB between 30°N and 6°N from the PetDB database (http://petdb.ldeo.columbia.edu/petdb). Northern hemisphere reference line (NHRL) after Hart (1984).

(0.76–0.83; Lundstrom et al., 2003). The (^{230}Th)/(^{232}Th) ratio is more variable with 0.82–0.85 for Henry Seamount and 1.15 for the 2011–2012 basanite, as compared to 1.06–1.23 for the other El Hierro samples. On an equiline diagram (Fig. 7a), our samples plot above the equiline with 3–5% of ^{230}Th excess over ^{238}U for Henry Seamount and 43% for the 2011–2012 basanite. This suggests that the two Henry Seamount samples have an upper age limit of <350 ka (five half-lives of ^{230}Th).

The (^{226}Ra)/(^{230}Th) activity ratios of the phonotephrite 22844-1A from Henry Seamount (1.26) and the 2011–2012 basanite (1.73) are in the range for Holocene rocks from El Hierro and other Canary Islands (Lundstrom et al., 2003), indicating significant ^{226}Ra—^{230}Th disequilibrium (Fig. 7b). This is expected for the 2011–2012 basanite and may indicate an age < 8 ka (five half-lives of ^{226}Ra) for the phonotephrite, also indicating that no age correction may be required for (^{238}U)/(^{230}Th). The (^{226}Ra)/(^{230}Th) ratio of 6.18 for the glassy ash sample 22841-1A, however, is unreasonably high for OIB data (Lundstrom, 2003; Bourdon and Sims, 2003; Saal and Van Orman, 2004). This sample also shows ^{234}U—^{238}U disequilibrium of 2.6%, whereas the other two samples are in ^{234}U—^{238}U equilibrium within analytical uncertainty (Table S5). We suggest that much of the ^{226}Ra excess of the ash sample reflects either contamination by seawater, or sediment remains in the small vesicles that were not removed by sample leaching (e.g., Chen et al., 1986), or minor hydrothermal alteration. Indeed, hydrothermal alteration by Ba-rich fluids and the formation of authigenic barite, which is a common host for Ra, are known to occur at Henry Seamount (Klügel et al., 2011).

4.5. Ar—Ar age dating

Despite repeated trials, dating of the samples by the ^{40}Ar/^{39}Ar method yielded usable results only for samples 22844-1A and 22844-1E (Table S6). The two most consistent step heating experiments and their potential implications on the ages of two samples are summarized in Fig. 8 in terms of age spectra and inverse isochron plots (yellow table heads in Table S6). Step heating of sample 22844-1A yielded an age spectrum with step ages between 0 ± 90 and 570 ± 90 ka (1 SD; Fig. 8a), excluding negative values and those with very low ^{39}Ar intensities (i.e. very large errors; Table S6). Selecting steps 3–6 and 8–10, with a total of 61% of the released ^{39}Ar$_K$, and forcing an inverse isochron through these steps (Fig. 8b), provides an inverse isochron age of 200 ± 100 ka at an exactly atmospheric initial ^{40}Ar/^{36}Ar of 298.6 ± 0.5 (atmospheric value: 298.56 ± 0.31). The large age uncertainty results from the high amount of non-radiogenic ^{40}Ar in each step, with the data plotting in the upper left of the inverse isochron diagram, whereas the age is calculated from the extrapolated x-axis intercept (Fig. 8c). Calculating a weighted mean average from these steps provides an age of 203 ± 38 ka for this sample, which we will include here as a best estimate. It is noted that the negative and zero-ages that also occurred during this experiment (hence at overall low ^{39}Ar signals; Table S6) might result from a slight over-correction on ^{40}Ar, either due to an undercorrection of ^{36}Ar through ^{36}Ar from Ca, or from an isobaric ^{36}Ar background. The reported best estimate age may thus be considered as a lower limit.

Step heating of sample 22844-1E provided two age groups of 403 ± 44 to 725 ± 95 ka, and 1.31 ± 0.47 to 2.57 ± 1.06 Ma, respectively. In an inverse isochron plot the data can be fitted by two inverse isochrons yielding ages of 190 ± 60 ka and 1.1 ± 0.9 Ma, at slightly superatmospheric initial ^{40}Ar/^{36}Ar ratios of 303.2 ± 0.6 and 301.4 ± 4.4, which suggests that all steps are compromised by a slight excess-^{40}Ar component (Fig. 8d). Recalculating the age of each step with the intercept value of steps 1–12 (303.2 ± 0.6) instead of an atmospheric value, i.e. taking into account the supposed excess component, provides a well-defined plateau for these steps with a mean weighted average of 190 ± 21 ka comprising 78% of the released ^{39}Ar$_K$ (Fig. 8e). This age is within error identical with the age of sample 22844-1A and is taken as best estimate for sample 22844-1E. It is emphasized, however, that the ages that result from the remaining 22% of released ^{39}Ar$_K$ at a virtually lower excess ^{40}Ar-component are significantly higher (Fig. 8d,e). As for sample 22844-1A, the suggested age of 190 ± 21 ka from steps 1–12 for sample 22844-1E may therefore define a lower age limit. Fig. 8f illustrates the location of the age-relevant x-axis intercepts of the two data subsets, and reports their statistical measures.

5. Discussion

The recovery of fresh and seemingly young basaltic samples from the top of Henry Seamount raises the question whether they were erupted from the Cretaceous seamount itself, or transported from an adjacent volcano, with nearby El Hierro island as the most plausible source. In the following sections we determine the provenance of the volcaniclastic

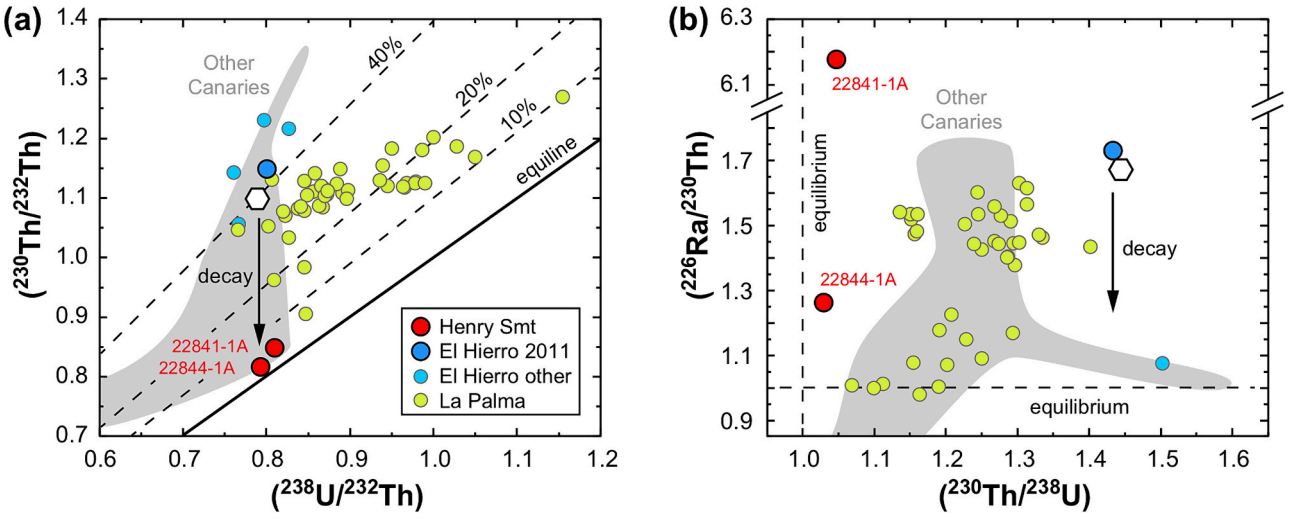

Fig. 7. (a) U—Th equiline diagram for two samples from Henry Seamount (sample numbers indicated) and one sample from the 2011–2012 El Hierro eruption, compared to literature data for Holocene and near-Holocene (<25 ka) eruptions from El Hierro, La Palma, and the other Canary Islands (Lundstrom et al., 2003; Johansen et al., 2005; Turner et al., 2015, 2017). Dashed lines with numbers indicate percent of ^{230}Th excess over ^{238}U, and downward arrow indicates ^{230}Th decay during ageing. The white hexagon represents a putative 4% peridotite melt as calculated by Turner et al. (2015); it plots very close to the 2011–2012 El Hierro basanite. (b) Diagram of (^{226}Ra)/(^{230}Th) versus (^{230}Th)/(^{238}U); symbols and data sources as in (a). Note the axis break for (^{226}Ra)/(^{230}Th) to display the extreme ^{226}Ra excess for sample 22841-1A.

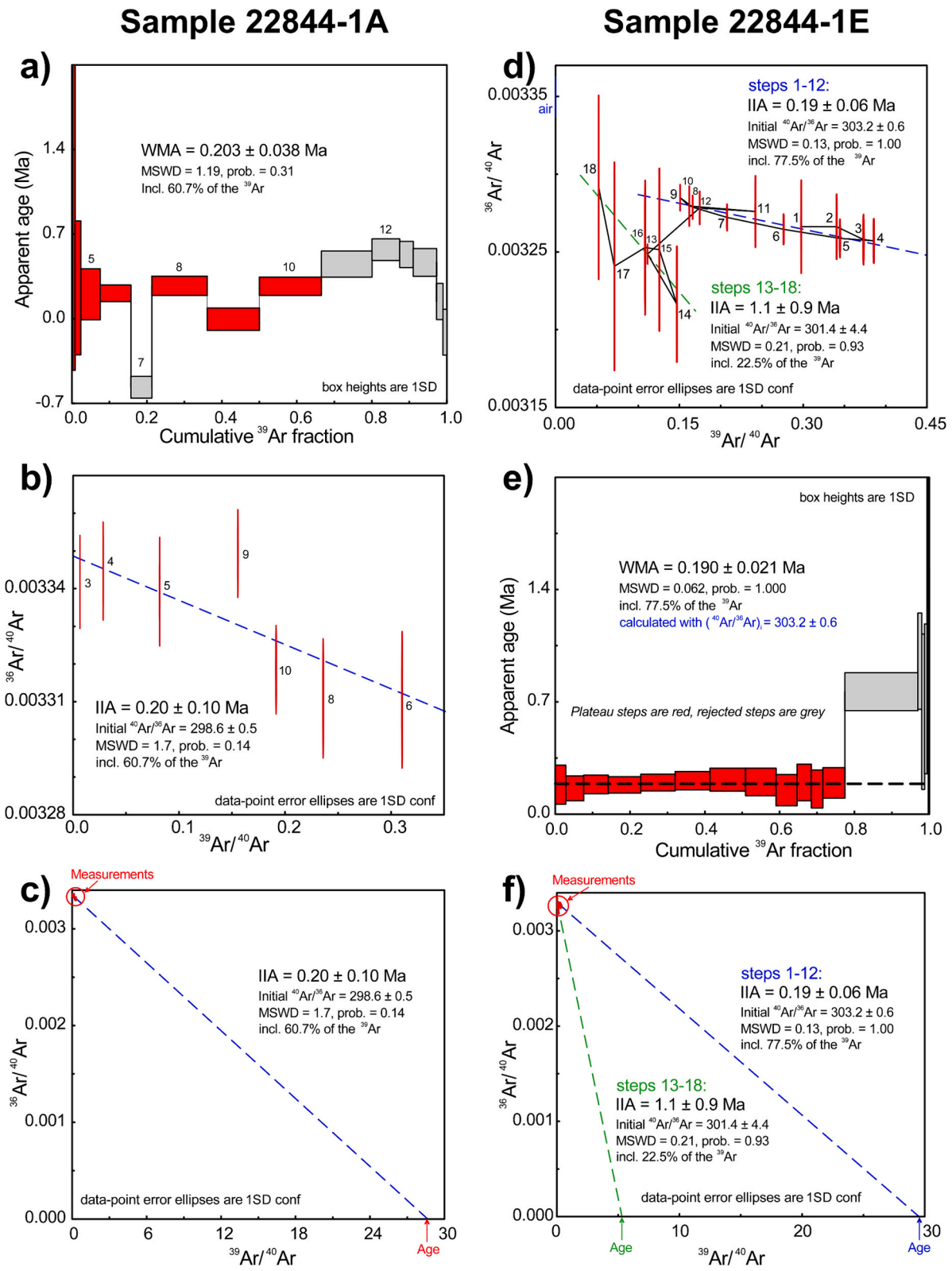

Fig. 8. Ar—Ar age spectra and inverse isochron plots of two step heating experiments on samples 22844-1A (a-c) and 22844-1E (d-e). WMA, weighted mean average; MSWD, mean square weighted deviation; SD, standard deviation. (a) No plateau is observed for sample 22844-1A, but calculating a WMA from steps 3–6 and 8–10 provides an age of 203 ± 38 ka (1 SD indicated). (b) Forcing an inverse isochron through the same steps yields an inverse isochron age (IIA) of 200 ± 100 ka at an atmospheric intercept of 298.6 ± 0.5 (c) The same data points as in (b), but rescaled to display the problem of very low amounts of radiogenic argon, leading to a large error on the x-axis intercept from which the age is calculated. (d) Two inverse isochrons with ages of 190 ± 60 ka and 1.1 ± 0.9 Ma can be forced through the data of sample 22844-1E, both having slightly superatmospheric $^{40}Ar/^{36}Ar$ intercepts of 303.2 ± 0.6 and 301.4 ± 4.4, respectively, suggesting the presence of excess argon in this sample. (e) Recalculating the ages of all temperature steps using an initial $^{40}Ar/^{36}Ar$ of 303.2 ± 0.6 as derived from steps 1–12 provides a well-defined plateau for these steps with a WMA age of 190 ± 21 ka. (f) Data points as in (d) but rescaled to display the x-axis intercepts from which two different ages result.

fragments, and discuss the possibility that many fragments were transported from El Hierro to Henry Seamount by a debris avalanche. We also assess the case for rejuvenated volcanism at the seamount.

5.1. Age of the samples from Henry Seamount

The ^{230}Th—^{238}U disequilibrium of sample 22841-1A indicates an upper age limit for type A ash of <350 ka. If the ^{230}Th excess of this sample at the time of eruption had been similar to that of Holocene El Hierro rocks (^{230}Th excess of 38–50%; Lundstrom et al., 2003), the calculated age would be in the range 230–260 ka. However, as there is not necessarily a genetic link to El Hierro, the initial ^{230}Th—^{238}U disequilibrium is not well constrained. For volcaniclastic lapilli, the best Ar—Ar age estimates are 190 ± 60 ka for sample 22844-1E (basalt fragment) and 203 ± 38 ka for sample 22844-1A (phonotephrite fragment). The latter age is consistent with a maximum age of 350 ka indicated by the ^{230}Th—^{238}U disequilibrium of that sample; for an initial ^{230}Th excess similar to Holocene El Hierro rocks an age range of 280–310 ka would be obtained. For sample 22844-1A such ages seem to be at odds with the observed ^{226}Ra excess, suggesting a significantly younger age of <8 ka (Fig. 7b), which would in turn imply an extremely small initial ^{230}Th excess of <3.2%. Considering that such a low initial ^{230}Th excess is not observed for any of the Canary Islands (Lundstrom et al., 2003), the Ar—Ar age estimate appears more plausible. This implies a significant disturbance of the ^{226}Ra—^{230}Th activity equilibrium of the phonotephrite sample during the last 8 ka, as was also inferred for the glassy ash sample 22841-1A (see above).

In summary, we estimate an age of 230–260 ka for type A ash and around 190–200 ka or older for the dated volcaniclastic lapilli. The ^{226}Ra—^{230}Th equilibrium of the investigated samples from Henry Seamount apparently became disturbed during the last 8 ka, possibly related to hydrothermal alteration by Ba-rich fluids as is documented by the recovery of authigenic barite and barite-impregnated rocks (Klügel et al., 2011; Klügel et al., 2020). Our findings are thus consistent with young (a few ka to a few tens of ka) hydrothermal activity at the seamount, but the cause for fluid circulation is not necessarily related to the eruption of significantly older type A ash.

5.2. Provenance of the volcaniclastic rocks from Henry Seamount

We have shown above that group 1 samples (type A ash and a dolerite fragment) show systematic compositional differences from El Hierro samples, notably lower concentrations of the most incompatible elements and distinct incompatible element ratios (Figs. 3, 4). These differences cannot be produced by fractionation of the observed macrocryst phases, but must reflect different magma source compositions and/or melting conditions. This argues against El Hierro as a possible origin of group 1 samples.

The petrographic characteristics and high S contents of type A ash strongly suggest an eruption at abyssal depths (e.g., Clague et al., 2003; Eissen et al., 2003; Freundt et al., 2021). The sideromelane fragments show blocky shapes and contain few microlites, indicative of rapid quenching (Fig. 2d). Vesicles are comparatively small and are surrounded by thick walls, suggesting dominance of hydroclastic over pyroclastic fragmentation. High ambient pressure at the eruptive site is indicated by the high S contents of the glasses, more specifically their S/K_2O ratios, as these strongly depend on S degassing and hence on pressure (Wallace and Edmonds, 2011; Ding et al., 2023). The highest S/K_2O ratios of type A ash glasses (0.19–0.20) exceed those for submarine El Hierro glasses erupted at up to 2100 m water depth (Stroncik et al., 2009), consistent with eruption at the depth from where the samples were taken (~3000 to 3200 m; Fig. 5b). The fact that S contents of type A ash glasses are below the extrapolated trend of El Hierro glasses at 3000 m water depth (Fig. 5a) does not necessarily indicate strong S degassing. It merely reflects that primary melts from Henry Seamount have lower S contents than El Hierro melts, which is in accordance with their overall lower contents of incompatible elements such as K (similarly incompatible as S), Th, and U (Fig. 4). The large range of S and S/K_2O in type A ash is likely the result of variable degassing during eruption, consistent with the variable vesicularity.

In summary, the combination of unique geochemical composition and eruption at considerable water depth suggest an origin of type A ash from Henry Seamount rather than from El Hierro. This interpretation is consistent with the observation during cruise M146 that type A ash layers were only recovered from the summit region of the seamount, where an eruptive site might have been located (Klügel and Shipboard Scientific Party, 2018). The angularity of most ash A particles with preserved sharp corners and bubble walls (Fig. 2d) suggests that they have undergone limited reworking (cf. Freundt et al., 2021).

In contrast to geochemical group 1 samples (mainly type A ash), group 2 samples from Henry Seamount are compositionally indistinguishable from El Hierro rocks. Many samples also have low S/K_2O ratios that are not consistent with eruption at >3000 m water depth (Fig. 5b), although submarine lavas can be degassed in some cases (Davis et al., 1991; Wanless et al., 2006). Whereas S/K_2O ratios of some samples are similar to glasses in submarine El Hierro samples from <1500 m water depth, those of other particles and of all lapilli-sized samples are similar to subaerially erupted rocks. In conjunction with the geochemical similarity of group 2 samples to El Hierro rocks, we conclude that most of them originated from subaerial or shallow submarine eruptions at El Hierro.

5.3. Evidence for flank collapse deposits

The inferred origin of most group 2 samples from El Hierro raises the question of how they could have been transported over 40 km distance to the top of Henry Seamount. A wind-driven subaerial transport may be conceivable for vesicular ash particles, but can be ruled out for dense centimeter-sized rock fragments. The only plausible mechanism is transport by a highly energetic submarine sediment flow from El Hierro. The angular to edge-rounded shapes of most group 2 fragments, and the presence of at least eight different lithologies, including fragments from apparently subaerial as well as submarine lava flows of variable degrees of alteration (Fig. 2), strongly suggest their derivation from a collapse event that sampled a larger part of the islands stratigraphy and probably formed a submarine debris avalanche and associated turbidity current (cf. Freundt et al., 2021).

The giant Las Playas II landslide at the southeast flank of El Hierro is the most likely source because it extended to the southeast and it is younger (145–176 ka; Gee et al., 2001a; Krastel et al., 2001; Masson et al., 2002) than our dated samples. The mapped deposits of this debris avalanche reach as close as ~10 km from Henry Seamount (Fig. 1b), but may extend considerably beyond this limit because very thin debris sheets are often poorly resolved by seismic profiling (Masson et al., 2002). Moreover, a sediment layer of approximately 5 m thickness overlies the landslide deposits and can mask thin debris layers (Masson et al., 2002). The underlying Las Playas I landslide (also named San Andres landslide; >176 ka), which extends even closer to Henry Seamount, was a gravitational slump associated with faults dated to between 176 ka and 545 ka (Gee et al., 2001a; Masson et al., 2002) and is thus potentially older than our dated samples.

According to Gee et al. (2001a) the Las Playas II debris avalanche was highly efficient, i.e., it had a high elevation difference (H) to runout length (L) ratio (H/L > 0.086) and a high area (A) to volume (V) ratio ($A/V^{2/3} > 98$), indicating rapid spread of the landslide mass. Rapid motion intensifies mixing with ambient seawater, which transforms parts of the avalanche into a highly mobile turbidity current (e.g., Garcia and Hull, 1994; Hunt et al., 2011, 2014). Being fed by sediment from the avalanche as long and as far out as it moves, particularly on the ~6° slope at 2 to 25 km offshore El Hierro (Fig. 1e), the turbidity current will behave as an igniting current (Parker, 1982) without the necessity to erode sediment from substrate. That such a turbidity current may run up

the 700 m to the top of Henry Seamount is supported by observations elsewhere. Turbidity currents derived from Hawaiian giant landslides transported volcanic sand for >265 km over the ~500 m high Hawaiian Arch (Garcia and Hull, 1994). Völker et al. (2008) found numerous turbidite layers on isolated seamounts rising up to 300 m from the Peru–Chile Trench, at 20 to 25 km distance from the sand after travelling upslope for several hundred to >1000 m.

Assuming a well-mixed, dilute turbidity current, Muck and Underwood (1990) argued that it could overflow a barrier height of 1.53 times the flow thickness (h) if 33% frictional energy losses are considered. For 700 m high Henry Seamount the minimum flow thickness would thus be 460 m. Assuming further a subcritical turbidity current (as may be expected on the low ~0.5° slope over the last 15 km in front of Henry Seamount; Fig. 1e) the maximum flow speed $u^2 < g'h$ would correspond to 5.4 to 13.3 m/s for suspended sediment concentrations of 0.5 to 3 wt % (Muck and Underwood, 1990; g' is reduced gravity). The turbidity current thickness is similar to values observed or estimated elsewhere, and the velocities lie fully in the range 8–25 m/s observed from submarine cable breaks (Muck and Underwood, 1990; Garcia and Hull, 1994; Piper et al., 1999; Felix, 2002; Völker et al., 2008; Heerema et al., 2020).

The volcaniclastic lapilli shown in Fig. 2e have settling velocities in water of 0.5–1 m/s (calculated after Dioguardi et al. (2018) using 2300 kg/m^3 clast density and shape factors 0.3 to 1), which must at least be balanced by turbulent shear velocity in order to facilitate suspension transport. Such shear velocities require mean current velocities of 8–16 m/s for a drag coefficient of 0.004 (Komar, 1985, Eq. 3). This estimate supports that a turbidity current able to overflow Henry Seamount was also able to carry the observed clasts to its top. We note, however, that there is large uncertainty in the drag coefficient (Komar, 1985), that particle concentrations >0.1% may influence flow behavior (Felix, 2002), and that tank experiments revealed some complexities of upslope flow (Marleau et al., 2014; Lombardi et al., 2015).

Recent direct monitoring of turbidity currents through continental-slope canyons yielded new insights into their internal structure and flow behavior. In these settings, fast flows appear to be driven by a frontal dense underflow with 10–30% sediment concentration (e.g., Paull et al., 2018; Talling et al., 2023). If such a dense, momentum-controlled flow was to surmount Henry Seamount it would need a minimum speed of 118 m/s (from equating kinetic with potential energy and ignoring frictional losses $u \geq (2gh)^{1/2}$), which is about an order of magnitude higher than observed velocities. The massive deposits expected from such dense flow (Talling et al., 2023) were not found on top of Henry Seamount, although we acknowledge that sampling was far from representative for the entire top region (Fig. 1c).

It is presently unclear in how far insights gained from erosive turbidity currents through canyons may be applicable to turbidity currents continuously fed from a moving submarine avalanche and spreading across open seafloor. In summary, although we used a simplistic approach, our interpretation of the volcaniclastic lapilli as fallout from a dilute current that partly overflowed Henry Seamount seems at least physically plausible.

The scenario of a debris-avalanche-derived turbidity current reaching the top of Henry Seamount can explain the superposition of clastic material from two widely separated sources: the dominant type A ash lithology apparently erupted from the seamount, and other heterolithologic clasts (of ash and lapilli size) derived from El Hierro. Our age estimates cannot reliably resolve the temporal order of their emplacement, but they suggest that type A ash was deposited prior to the Las Playas II landslide. In that case the observed mingling of the different components likely reflects violent transport and emplacement conditions of the collapse-induced turbidity current as it crossed the seamount summit. Here, it partly mixed its fragmental load with resident sediment including type A ash. In the less likely case of type A ash eruption long after the landslide occurred, mingling may have been caused either by entrainment of landslide clasts at the eruption site, or by local mass flows that formed on steep slope sections (Fig. 1e) during or after the respective eruption.

5.4. Mantle sources of Henry Seamount and El Hierro volcanism

The alkaline to transitional basalts of group 1 contain moderately forsteritic olivine macrocrysts ($Fo_{79.5–82.6}$; Kahl et al., 2022), have moderate MgO contents around 7 wt%, and are low in Ni (67–101 μg/g) and Cr (116–162 μg/g) concentrations (Table S3). Thus, they are not primitive melts but have undergone significant fractionation of olivine and minor Cr-rich spinel. Compared to rocks from El Hierro, group 1 samples have distinctively lower contents of highly incompatible elements and flatter REE patterns (i.e., lower La/Lu ratios; Fig. 4). These geochemical differences cannot be produced by crystal fractionation but reflect distinct melting conditions and/or compositions of the mantle source. The source beneath El Hierro is thought to be a mixture of garnet-bearing peridotite and recycled oceanic crust, likely present as garnet pyroxenite/eclogite, but details on lithology and mixing proportions are debated (e.g., Gurenko et al., 2009; Day et al., 2010) and are beyond the scope of this contribution.

A unique indicator for pyroxenite-derived melts, that is not sensitive to different melting scenarios, is a La/Nb ratio <<1 (Stracke and Bourdon, 2009). The distinctively low La/Nb ratios of group 1 samples (Fig. 9a) could therefore reflect a higher proportion of pyroxenite in the mixed melts, as compared to El Hierro and group 2 samples. However, the opposite would be true by considering the high Ba/Th ratios of group 1 samples, as these suggest a larger peridotite proportion (Stracke and Bourdon, 2009). Another discrimination between peridotite- and pyroxenite-derived melts is provided by the FC3MS parameter (FeO/CaO-3*MgO/SiO_2, in wt%) of Yang and Zhou (2013). The FC3MS values of peridotite-derived melts with MgO > 7.5 wt% or Mg# > 50 are generally below 0.65, whereas most pyroxenite-derived melts have significantly higher FC3MS at given Mg# or alkali content. The FC3MS values of the most magnesian group 1 samples (Mg# ~50.5) are around 0.5, well below those of El Hierro samples with similar Mg# (0.75–1.2). This would suggest a large peridotite proportion in primary melts for group 1 samples and a dominant pyroxenite proportion in those for El Hierro and group 2 samples.

Another distinctive source-related feature of group 1 samples are their extreme ratios of highly incompatible elements, such as high (Nb, Ta)/U and Ba/Th, and low La/(Nb,Ta) (Figs. 3b, 9). The Nb/U of most samples is within 80 ± 10, well above Nb/U of El Hierro and group 2 samples, most of which are within the typical mantle range for oceanic basalts of 47 ± 10 (Hofmann et al., 1986). Overall, the sample suite from El Hierro and Henry Seamount shows good correlations of Nb/U with Ba/(La,U,Th), La/(Nb,Ta,Th,U,Sm,Yb), and K/U, and also a wide range for each of these ratios (Fig. 9). These observations may be explained by variable proportions and/or compositions of peridotite- and pyroxenite-derived melts that mix during melt extraction from the mantle source (Stracke and Bourdon, 2009). The lack of correlation between these element ratios and radiogenic isotope ratios such as $^{143}Nd/^{144}Nd$ for El Hierro lavas (Day et al., 2010; Klügel et al., 2017) suggests that melts are extracted from a restricted depth interval rather than from a long melting column (Stracke and Bourdon, 2009). In summary, major and trace element data of our sample suite are consistent with a pyroxenite component in the melt source, but observed systematic variations are not unequivocally explained by variable proportions of this component.

As an alternative, the geochemical peculiarities of group 1 samples may reflect lithospheric melting processes. High (Nb,Ta)/U, Ba/Th, and low La/(Nb,Ta) are characteristic amphibole signatures, as this mineral phase can strongly affect these ratios (Adam and Green, 2006; Viccaro et al., 2007; Pilet et al., 2008). High Nb/U ratios are not uncommon for Canary Island lavas, and were attributed by Lundstrom et al. (2003) to melting of metasomatic amphibole-rich veins or cumulates in the lithospheric mantle. A similar mechanism was invoked to explain systematic variations of Nb/U, Ba/Th, and La/Nb during the geochemical

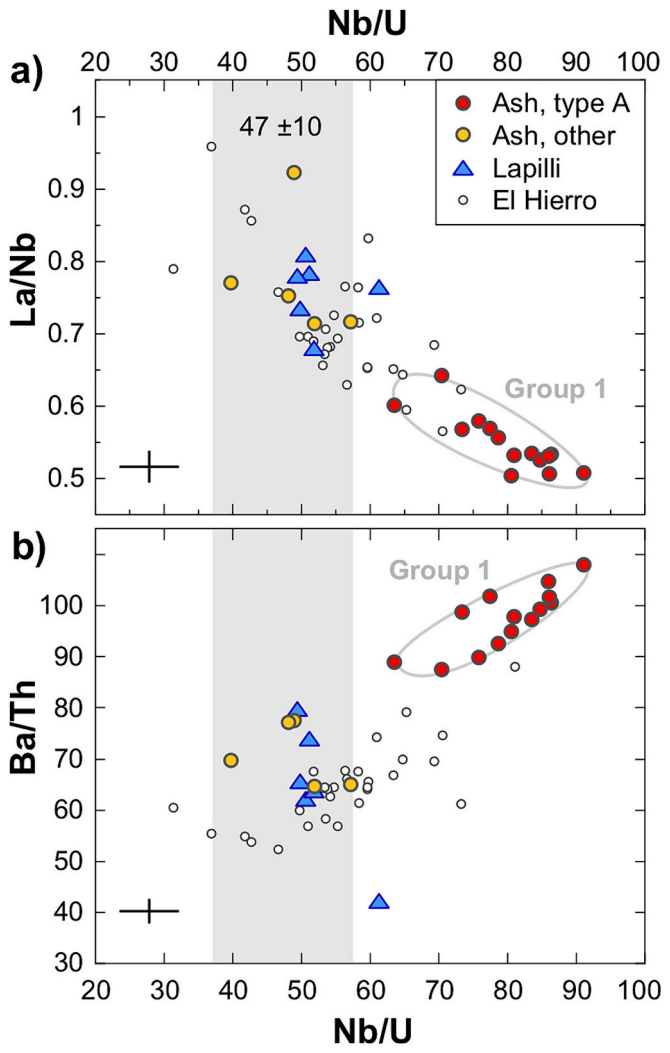

Fig. 9. Ratio-ratio diagrams of samples with >4 wt% MgO to place constraints on the mantle source. Group 1 samples represented by type A ash, group 2 by all other Henry Seamount samples. Symbols as in Fig. 3; error bars indicate mean analytical precision (2 SD). Correlations of Nb/U with (a) La/Nb and (b) Ba/Th suggest a possible role of amphibole in the mantle source. Shaded field indicates the typical mantle range of Nb/U for oceanic basalts (47 ± 10; Hofmann et al., 1986).

evolution of adjacent La Palma island (Klügel et al., 2017). Amphibole veins can be introduced by earlier magmatic stages when percolating or channelized asthenospheric melts produce partial crystal precipitates (cumulates) in the colder lithospheric mantle (e.g., Harte et al., 1993). When these low-solidus veins and the enclosing high-solidus peridotite melt to variable degrees at a later stage, correlations between said element ratios (Fig. 9) are expected (Pilet et al., 2008). This model implies shallower peridotite melting conditions of group 1 samples compared to samples with "normal" Nb/U, which would be in accordance with the inferred involvement of spinel lherzolite in the melting process (see above). Alternatively, the amphibole signatures may also be imprinted in the shallower lithosphere through assimilation of amphibole in cumulates or crystal mush by rising asthenospheric melts.

5.5. Causes for rejuvenated volcanism at Henry Seamount

The occurrence of rejuvenated volcanism at Henry Seamount during the shield-building stage of El Hierro, the small distance between both edifices, and overlapping Sr—Nd—Pb isotope data (Fig. 6), suggest some similarities in their mantle source. Renewed volcanic activity at Henry Seamount after its formation at 126 Ma is thus likely related to the melting anomaly giving rise to the Canary Archipelago. The current focus of the Canary hotspot is thought to be located between La Palma and El Hierro (Geldmacher et al., 2005), yet seismic studies suggest the ubiquitous presence of melt in a low-velocity layer beneath most of the archipelago (Martinez-Arevalo et al., 2013). The question arises as to why young volcanic activity specifically occurs at Henry Seamount? Its location south-southeast of El Hierro cannot be easily explained by plate motions, unless additional mantle convection is invoked (Negredo et al., 2022). We propose that enhanced melt production beneath the seamount is related to the presence of locally metasomatized lithosphere as discussed above. This may have occurred during the Cretaceous magmatic activity that produced Henry Seamount, as this was necessarily accompanied by substantial interactions between rising basaltic melts and lithospheric mantle, including crystallization of amphibole-rich veins (Harte et al., 1993). When the lower lithosphere became reheated by the Canary hotspot, possibly aided by small volumes of rising asthenospheric melts, the metasomatized low-solidus zones also underwent melting. Increasing temperature and melt fraction facilitated further ascent and accumulation of the melts, and ultimately eruption.

The model involving the melting of ancient lithospheric amphibole is not in conflict with the observed Nd—Pb isotope similarity between El Hierro samples and group 1 Henry Seamount samples (Fig. 6). If the inferred amphibole veins had isotopic compositions not much different from the present-day El Hierro source, a mixture of lithospheric and asthenospheric melts would retain the Nd—Pb isotope signatures. Calculations show that this is possible even if the metasomatic amphiboles crystallized from the same melts that produced Henry Seamount trachytes 126 Ma ago. Based on the average compositions of the trachytes (Klügel et al., 2011) we calculated their initial Nd—Pb isotope ratios and the trace element compositions of amphiboles crystallized from such melts. By tentatively mixing present-day melts of these amphiboles with a representative near-primitive El Hierro melt in a 1:1 ratio, we obtain a Nd—Pb isotopic composition very similar to group 1 samples; details of the calculations are given in the Supplementary Information.

An intriguing property of predominant type A ash from group 1 is the chemical variety of the glasses, with considerable variations in incompatible element ratios and mutual correlations as discussed above (Fig. 9). Similar relations exist between, e.g., MgO, Ni and Cr. These variations cannot reflect chemical gradients in the vicinity of microlites and macrocrysts, as this would not affect the incompatible element ratios. It rather appears that the rising basaltic magma was chemically zoned. This is possible if there was no homogenizing magma reservoir at depth, which would agree with the small volume erupted (Klügel et al., 2020). Alternatively, the rising magma may have become chemically modified during the eruption by, e.g., assimilation of wall-rock. In this case, amphibole was likely involved in the process.

The inferred rejuvenated volcanic activity at Henry Seamount differs in some respects from the "classic" situation at Hawaii. For Hawaiian volcanoes, the earlier edifice-building stages and the rejuvenated stage are related to the same hotspot underlying a fast-moving lithosphere plate. At Henry Seamount these stages appear not to be related at all: the earlier volcanism that built the seamount merely pre-conditioned a slow-moving lithosphere via metasomatism, making it more fusible when the Canary hotspot was approached. As a consequence, rejuvenated volcanism can occur even after a hiatus of >120 million years. Another difference is the highly SiO_2-undersaturated, trace element-enriched and isotopically depleted character of rejuvenated lavas at Hawaii, when compared to shield-building lavas (e.g., Clague, 1987). In contrast, group 1 samples of Henry seamount are less alkalic and less incompatible element-enriched than contemporaneous El Hierro lavas, and are isotopically similar.

The inferred rejuvenated volcanic activity at Henry Seamount appears not to be restricted to the eruption of type A ash. Seismic data show zones of amplitude blanking between 5 and 25 km from the base of the seamount with upward bending of adjacent reflectors (Klügel et al.,

2020). These features closely resemble hydrothermal domes that result from deeper sill-like magmatic intrusions and related hydrothermal activity (Berndt et al., 2016; Medialdea et al., 2017). As these blanking zones affect some 100 m of sediments that are overlying the basement, the inferred intrusive activity must be considerably younger than the seamount and may be related to the rejuvenated volcanism.

6. Conclusions

- The summit region of Henry Seamount contains at least one layer of heterolithologic volcaniclastic ash and lapilli, overlain by centimeters to decimeters of pelagic sediment. The dominant lithology (glassy type A ash) and a number of other samples are relatively fresh, but overall the sample suite shows highly variable degrees of alteration.
- Based on major and trace element compositions the samples fall into two groups. Group 1 samples, represented by type A ash as the dominant lithology, are geochemically different from El Hierro and have elevated S concentrations in matrix glass. They were erupted at considerable water depth, consistent with an origin from Henry Seamount. Group 2 samples are geochemically similar to volcanic rocks from El Hierro and have low S concentrations, suggesting an origin from this island.
- Ar—Ar dating of two group 2 samples suggests minimum ages around 190–200 ka. The transport of group 2 samples from El Hierro to Henry Seamount must have occurred by turbidity currents derived from a debris avalanche, the 145–176 ka Las Playas II avalanche being the most likely candidate as it is younger than the transported rocks. This implies a runup of up to 700 m even for centimeter-sized basaltic clasts after up to 40 km of lateral transport. Mingling and reworking of type A ash and local sediment by the turbidity current may explain the lack of a discernible eruption center on top of Henry Seamount.
- Uranium-series disequilibria suggest an age of <350 ka for type A ash, possibly 230–260 ka, which indicates rejuvenated volcanic activity of the Cretaceous seamount. This implies that rejuvenated volcanism at seamounts can occur even after a hiatus of >120 million years. At Henry Seamount, rejuvenated activity seems to be related to the Canary hotspot, with renewed melt production beneath the seamount as a consequence of earlier enrichment of the lithosphere by metasomatic amphibole. In contrast to the situation at Hawaiian volcanoes, the earlier and rejuvenated volcanic activity are not necessarily related to the same stationary melting anomaly, even at slow plate motions prevailing in the Eastern Atlantic.

Funding

Our research was funded by the Deutsche Forschungsgemeinschaft (DFG, grant KL1313/18-1, project number 418368213), and GEOMAR institutional funds for the Sr-Nd-Pb isotope analysis. MR was funded by the DFG under Germany's Excellence Strategy – EXC-2077 – 390741603.

CRediT authorship contribution statement

Andreas Klügel: Writing – original draft, Project administration, Methodology, Investigation, Formal analysis, Data curation, Conceptualization. **Folkmar Hauff:** Writing – review & editing, Methodology, Investigation, Formal analysis. **Christoph Beier:** Writing – review & editing, Methodology, Investigation, Formal analysis. **Jörg A. Pfänder:** Writing – review & editing, Validation, Methodology, Investigation, Formal analysis. **Armin Freundt:** Writing – review & editing, Validation, Formal analysis. **Miriam Römer:** Writing – review & editing, Methodology, Investigation. **Milena Schönhofen-Romer:** Writing – review & editing, Investigation.

Declaration of competing interest

The authors declare that they have no known competing financial interests or personal relationships that could have appeared to influence the work reported in this paper.

Data availability

The research data for this article (Supplementary Tables) are available at: Klügel (2024), "Henry Seamount Research Data", Mendeley Data, V1, doi: 10.17632/6y4pkv2j55.1.

Acknowledgments

We are grateful to Captain R. Hammacher and the crew and shipboard scientific party of R/V *Meteor* cruise M146 for excellent work, and the Leitstelle Deutsche Forschungsschiffe for overall support. We acknowledge A. Dosseto, A. Francke, J. Sikdar and S. P. Turner for their help and support during the U-series analysis, E. Ranta for running models of S degassing, and B. Sperner for support of the Ar—Ar measurements, data reduction, age calculation and interpretation. Special thanks go to the team of the LVR-15 Reactor Services Division of the Research Centre in Řež, Czech Republik, for performing the neutron irradiation of the samples for Ar—Ar dating on basis of an open-access agreement. The constructive comments by reviewer Neil Mitchell helped to improve the manuscript and are greatly appreciated.

Appendix A. Supplementary data

Supplementary data to this article can be found online at https://doi.org/10.1016/j.margeo.2024.107301.

References

Abratis, M., Schmincke, H.U., Hansteen, T.H., 2002. Composition and evolution of submarine volcanic rocks from the central and western Canary Islands. Int. J. Earth Sci. 91, 562–582.

Adam, J., Green, T., 2006. Trace element partitioning between mica- and amphibole-bearing garnet lherzolite and hydrous basanitic melt: 1. Experimental results and the investigation of controls on partitioning behaviour. Contrib. Mineral. Petrol. 152, 1–17. https://doi.org/10.1007/s00410-00006-00085-00414.

Beier, C., Turner, S.P., Sinton, J.M., Gill, J.B., 2010. Influence of subducted components on back-arc melting dynamics in the Manus Basin. Geochem. Geophys. Geosyst. 11 https://doi.org/10.1029/2010GC003037.

Beier, C., Vanderkluysen, L., Regelous, M., Mahoney, J.J., Garbe-Schönberg, D., 2011. Lithospheric control on geochemical composition along the Louisville Seamount Chain. Geochem. Geophys. Geosyst. 12 https://doi.org/10.1029/2011GC003690.

Berndt, C., Hensen, C., Mortera-Gutierrez, C., Sarkar, S., Geilert, S., Schmidt, M., Liebetrau, V., Kipfer, R., Scholz, F., Doll, M., Muff, S., Karstens, J., Planke, S., Petersen, S., Böttner, C., Chi, W.C., Moser, M., Behrendt, R., Fiskal, A., Lever, M.A., Su, C.C., Deng, L., Brennwald, M.S., Lizarralde, D., 2016. Rifting under steam—how rift magmatism triggers methane venting from sedimentary basins. Geology 44, 767–770.

Bourdon, B., Sims, K.W.W., 2003. U-series Constraints on Intraplate Basaltic Magmatism. Rev. Mineral. Geochem. 52, 215–254.

Carracedo, J.C., 1999. Growth, structure, instability and collapse of Canarian volcanoes and comparisons with Hawaiian volcanoes. J. Volcanol. Geotherm. Res. 94, 1–19.

Carracedo, J.C., Badiola, E.R., Guillou, H., de La Nuez, J., Pérez Torrado, F.J., 2001. Geology and volcanology of La Palma and El Hierro, Western Canaries. Estudios Geol. 57, 175–273.

Chen, J.H., Lawrence Edwards, R., Wasserburg, G.J., 1986. ^{238}U, ^{234}U and ^{232}Th in seawater. Earth Planet. Sci. Lett. 80, 241–251.

Clague, D.A., 1987. Hawaiian alkaline volcanism. Geol. Soc. Lond. Spec. Publ. 30, 227–252.

Clague, D.A., Dalrymple, G.B., 1987. The Hawaiian-Emperor volcanic chain. In: Decker, R.W., Wright, T.W., Stauffer, P.H. (Eds.), Volcanism in Hawaii, US Geol. Surv. Prof. Pap. 1350, pp. 5–54.

Clague, D.A., Batiza, R., Head III, J.W., Davis, A.S., 2003. Pyroclastic and hydroclastic deposits on Loihi Seamount, Hawaii. In: White, J.D.L., Smellie, J.L., Clague, D.A. (Eds.), Explosive Subaqueous Volcanism. American Geophysical Union, Washington DC, pp. 73–95.

Davis, A.S., Clague, D.A., 2006. Volcaniclastic deposits from the North Arch volcanic field, Hawaii: explosive fragmentation of alkalic lava at abyssal depths. Bull. Volcanol. 68, 294–307.

Davis, A.S., Clague, D.A., Schulz, M.S., Hein, J.R., 1991. Low sulfur content in submarine lavas: an unreliable indicator of subaerial eruption. Geology 19, 750–753.

Day, S.J., Carracedo, J.C., Guillou, H., 1997. Age and geometry of an aborted rift collapse: the San Andres fault system, El Hierro, Canary Islands. Geol. Mag. 134, 523 ±537. Geol. Mag. 134, 523–537.
Day, J.M.D., Pearson, D.G., Macpherson, C.G., Lowry, D., Carracedo, J.C., 2010. Evidence for distinct proportions of subducted oceanic crust and lithosphere in HIMU-type mantle beneath El Hierro and La Palma, Canary Islands. Geochim. Cosmochim. Acta 74, 6565–6589.
Ding, S., Plank, T., Wallace, P.J., Rasmussen, D.J., 2023. Sulfur_X: a Model of Sulfur Degassing during Magma Ascent. Geochem. Geophys. Geosyst. 24 https://doi.org/10.1029/2022GC010552.
Dioguardi, F., Mele, D., Dellino, P., 2018. A new one-equation model of fluid drag for irregularly shaped particles valid over a wide range of Reynolds Number. J. Geophys. Res. 123, 144–156. https://doi.org/10.1002/2017JB014926.
Dorais, M.J., Buchs, D.M., 2019. Mineralogical characterization of rejuvenated magmatism at Burton Guyot. Louisville Seamount Trail. Contrib. Mineral. Petrol. 174, 66.
Dosseto, A., Turner, S.P., Douglas, G.B., 2006. Uranium-series isotopes in colloids and suspended sediments: Timescale for sediment production and transport in the Murray–Darling River system. Earth Planet. Sci. Lett. 246, 418–431.
Eissen, J.-P., Fouquet, Y., Hardy, D., Ondréas, H., 2003. Recent MORB Volcaniclastic explosive deposits formed between 500 and 1750 m.b.s.l. on the axis of the Mid-Atlantic Ridge, south of the Azores. In: White, J.D.L., Smellie, J.L., Clague, D.A. (Eds.), Explosive Subaqueous Volcanism. American Geophysical Union, Washington DC, pp. 143–166.
Felix, M., 2002. Flow structure of turbidity currents. Sedimentology 49, 397–419.
Francke, A., Carney, S., Wilcox, P., Dosseto, A., 2018. Sample preparation for determination of comminution ages in lacustrine and marine sediments. Chem. Geol. 479, 123–135.
Freundt, A., Schindlbeck-Belo, J.C., Kutterolf, S., Hopkins, J.L., 2021. Tephra layers in the marine environment: A review of properties and emplacement processes. In: Di Capua, A., De Rosa, R., Kereszturi, G., Le Pera, E., Rosi, M., Watt, S.F.L. (Eds.), Volcanic Processes in the Sedimentary Record: When Volcanoes Meet the Environment. Geological Society, London, Special Publications, pp. 1–43.
Garcia, M.O., Hull, D.M., 1994. Turbidites from giant Hawaiian landslides: results from Ocean Drilling Program Site 842. Geology 22, 159–162.
Gee, M.J.R., Watts, A.B., Masson, D.G., Mitchell, N.C., 2001a. Landslides and the evolution of El Hierro in the Canary Islands. Mar. Geol. 177, 271–293.
Gee, M.J.R., Masson, D.G., Watts, A.B., Mitchell, N.C., 2001b. Offshore continuation of volcanic rift zones, El Hierro, Canary Islands. J. Volcanol. Geotherm. Res. 105, 107–119.
Geldmacher, J., Hoernle, K., Bogaard, P., Zankl, G., Garbe-Schönberg, D., 2001. Earlier history of the ≥70-Ma-old Canary hotspot based on the temporal and geochemical evolution of the Selvagen Archipelago and neighboring seamounts in the eastern North Atlantic. J. Volcanol. Geotherm. Res. 111, 55–87.
Geldmacher, J., Hoernle, K., Bogaard, P.V.D., Duggen, S., Werner, R., 2005. New $^{40}Ar/^{39}Ar$ age and geochemical data from seamounts in the Canary and Madeira volcanic provinces: support for the mantle plume hypothesis. Earth Planet. Sci. Lett. 237, 85–101.
Guillou, H., Carracedo, J.C., Perez Torrado, F.J., Rodrıguez Badiola, E., 1996. K–Ar ages and magnetic stratigraphy of a hotspot-induced, fast grown oceanic island: El Hierro, Canary Islands. J. Volcanol. Geotherm. Res. 73, 141–155.
Gurenko, A.A., Hoernle, K.A., Hauff, F., Schmincke, H.U., Han, D., Miura, Y.N., Kaneoka, I., 2006. Major, trace element and Nd–Sr–Pb–O–He–Ar isotope signatures of shield stage lavas from the central and western Canary Islands: Insights into mantle and crustal processes. Chem. Geol. 233, 75–112.
Gurenko, A.A., Sobolev, A.V., Hoernle, K.A., Hauff, F., Schmincke, H.U., 2009. Enriched, HIMU-type peridotite and depleted recycled pyroxenite in the Canary plume: a mixed-up mantle. Earth Planet. Sci. Lett. 277, 514–524.
Hart, S.R., 1984. A large-scale isotope anomaly in the southern hemisphere mantle. Nature 309, 753–757.
Harte, B., Hunter, R.H., Kinny, P.D., 1993. Melt geometry, movement and crystallization, in relation to mantle dykes, veins and metasomatism. Philos. Trans. R. Soc. London A 342, 1–21.
Hauff, F., Hoernle, K., Gill, J., Werner, R., Timm, C., Garbe-Schönberg, D., Gutjahr, M., Jung, S., 2021. R/V SONNE Cruise SO255 "VITIAZ": an integrated major element, trace element and Sr-Nd-Pb-Hf isotope data set of volcanic rocks from the Colville and Kermadec Ridges. In: The Quaternary Kermadec volcanic front and the Havre Trough backarc basin, Version 1.0. Interdisciplinary Earth Data Alliance (IEDA). https://doi.org/10.26022/IEDA/111723.
Hausen, H., 1972. Outlines of the Geology of Hierro (Canary Islands). Comm. Phys. Math. Finn. Acad. Sci. 43, 65–148.
Heerema, C.J., Talling, P.J., Cartigny, M.J., Paull, C.K., Bailey, L., Simmons, S.M., Parsons, D.R., Clare, M.A., Gwiazda, R., Lundsten, E., Anderson, K., Maier, K.L., Xu, J.P., Sumner, E.J., Rosenberger, K., Gales, J., McGann, M., Carter, L., Pope, E., Monterey Coordinated Canyon Experiments (CCE) Team, 2020. What determines the downstream evolution of turbidity currents? Earth Planet. Sci. Lett. 532, 116023 https://doi.org/10.1016/j.epsl.2019.116023.
Hillier, J.K., Watts, A., 2007. Global distribution of seamounts from ship-track bathymetry data. Geophys. Res. Lett. 34, L13304. https://doi.org/10.1029/2007GL029874.
Hoernle, K., 1998. Geochemistry of Jurassic oceanic crust beneath Gran Canaria (Canary Islands); implications for crustal recycling and assimilation. J. Petrol. 395, 859–880.
Hoernle, K., Schmincke, H.U., 1993. The role of partial melting in the 15-Ma geochemical evolution of Gran Canaria: a blob model for the Canary hotspot. J. Petrol. 34, 599–626.
Hoernle, K., Tilton, G., Schmincke, H.U., 1991. Sr-Nd-Pb isotopic evolution of Gran Canaria: evidence for shallow enriched mantle beneath the Canary Islands. Earth Planet. Sci. Lett. 106, 44–63.
Hofmann, A.W., Jochum, K.P., Seufert, M., White, W.M., 1986. Nb and Pb in oceanic basalts: New constraints on mantle evolution. Earth Planet. Sci. Lett. 79, 33–45.
Holcomb, R.T., Searle, R.C., 1991. Large landslides from oceanic volcanoes. Mar. Geotechnol. 10, 19–32.
Hunt, J.E., Wynn, R.B., Masson, D.G., Talling, P.J., Teagle, D.A.H., 2011. Sedimentological and geochemical evidence for multistage failure of volcanic island landslides: a case study from Icod landslide on North Tenerife, Canary Islands. Geochem. Geophys. Geosyst. 12 https://doi.org/10.1029/2011GC003740.
Hunt, J.E., Talling, P.J., Clare, M.A., Jarvis, I., Wynn, R.B., 2014. Long-term (17 Ma) turbidite record of the timing and frequency of large flank collapses of the Canary Islands. Geochem. Geophys. Geosyst. 15, 3322–3345. https://doi.org/10.1002/2014GC005232.
Jarosewich, E.J., Nelen, J.A., Norberg, J.A., 1980. Reference samples for electron microprobe analysis. Geostand. Newslett. 4, 43-47. Correction 44, 257–258.
Jochum, K.P., Willbold, M., Raczek, I., Stoll, B., Herwig, K., 2005. Chemical Characterisation of the USGS Reference Glasses GSA-1G, GSC-1G, GSD-1G, GSE-1G, BCR-2G, BHVO-2G and BIR-1G using EPMA, ID-TIMS, ID-ICP-MS and LA-ICP-MS. Geostand. Geoanal. Res. 29, 285–302.
Johansen, T.S., Hauff, F., Hoernle, K., Klügel, A., Kokfelt, T.F., 2005. Basanite to phonolite differentiation within 1550-1750 yr: U-Th-Ra isotopic evidence from the a. D. 1585 eruption on La Palma, Canary Islands. Geology 33, 897–900.
Kahl, W.-A., Klügel, A., Bach, W., Mangir Murshed, M., 2022. Enhanced weathering in the seabed: Rapid olivine dissolution and iron sulfide formation in submarine volcanic ash. Am. Mineral. 107, 1668–1680.
Klügel, Andreas, 2024. Henry Seamount Research Data. Mendeley Data V1. https://doi.org/10.17632/6y4pkv2j55.1.
Klügel, A., Hansteen, T.H., Bogaard, P.V.D., Strauss, H., Hauff, F., 2011. Holocene fluid venting at an extinct cretaceous seamount, Canary archipelago. Geology 39, 855–858.
Klügel, A., Shipboard Scientific Party, 2018. METEOR Fahrtbericht / Cruise Report M146, Henry Seamount Seepage Exploration (HESSE), Recife (Brazil) - Las Palmas de Gran Canaria (Spain), March 17–April 16, 2018, METEOR-Berichte. Gutachterpanel Forschungsschiffe, Bonn, pp. 1–88. https://doi.org/10.2312/cr_m146.
Klügel, A., Galipp, K., Hoernle, K., Hauff, F., Groom, S., 2017. Geochemical and Volcanological Evolution of La Palma, Canary Islands. J. Petrol. 58, 1227–1248.
Klügel, A., Day, S., Schmid, M., Faria, B., 2020. Magma Plumbing during the 2014–2015 Eruption of Fogo (Cape Verde Islands). Front. Earth Sci. 8, 157. https://doi.org/10.3389/feart.2020.00157.
Klügel, A., Römer, M., Wintersteller, P., Lenz, K.-F., Krastel, S., Villinger, H., Kaul, N., 2021. Bathymetric and Seismic Data, Heat Flow Data, and Age Constraints of Le Gouic Seamount, Northeastern Atlantic. Front. Mar. Sci. 8, 617927 https://doi.org/10.3389/fmars.2021.617927.
Klügel, A., Albers, E., Hansteen, T.H., 2022. Mantle and Crustal Xenoliths in a Tephriphonolite from La Palma (Canary Islands): Implications for Phonolite Formation at Oceanic Island Volcanoes. Front. Earth Sci. 10, 761902 https://doi.org/10.3389/feart.2022.761902.
Komar, P.D., 1985. The hydraulic interpretation of turbidites from their grain sizes and sedimentary structures. Sedimentology 32, 395–407.
Krastel, S., Schmincke, H.-U., Jacobs, C.L., Rihm, R., Le Bas, T.P., Alibés, B., 2001. Submarine landslides around the Canary Islands. J. Geophys. Res. 106, 3977–3997.
Lee, J.-Y., Marti, K., Severinghaus, J.P., Kawamura, K., Yoo, H.-S., Lee, J.B., Kim, J.S., 2006. A redetermination of the isotopic abundances of atmospheric Ar. Geochim. Cosmochim. Acta 70, 4507–4512.
León, R., Somoza, L., Urgeles, R., Medialdea, T., Ferrer, M., Biain, A., García-Crespo, J., Mediato, J.F., Galindo, I., Yepes, J., González, F.J., Gimenez-Moreno, J., 2017. Multi-event oceanic island landslides: New onshore-offshore insights from El Hierro Island, Canary Archipelago. Mar. Geol. 393, 156–175.
Lombardi, V., Adduce, C., Sciortino, G., La Rocca, M., 2015. Gravity currents flowing upslope: Laboratory experiments and shallow-water simulations. Phys. Fluids 27, 016602. https://doi.org/10.1063/1.4905305.
Longpré, M.A., Chadwick, J.P., Wijbrans, J., Iping, R., 2011. Age of the El Golfo debris avalanche, El Hierro (Canary Islands): New constraints from laser and furnace $^{40}Ar/^{39}Ar$ dating. J. Volcanol. Geotherm. Res. 203, 76–80.
Longpré, M.A., Klügel, A., Diehl, A., Stix, J., 2014. Mixing in mantle magma reservoirs prior to and during the 2011–2012 eruption at El Hierro, Canary Islands. Geology 42, 315–318.
Ludwig, K., 2008. Isoplot 3.60: Berkeley geochronology center. Special Publication 4, 106.
Lundstrom, C.C., 2003. Uranium-series Disequilibria in Mid-ocean Ridge Basalts: Observations and Models of Basalt Genesis. Rev. Mineral. Geochem. 52, 175–214.
Lundstrom, C.C., Hoernle, K.A., Gill, J., 2003. U-series disequilibria in volcanic rocks from the Canary Islands: Plume versus lithospheric melting. Geochim. Cosmochim. Acta 67, 4153–4177.
Marleau, L.J., Flynn, M.R., Sutherland, B.R., 2014. Gravity currents propagating up a slope. Phys. Fluids 26, 046605. https://doi.org/10.1063/1.4872222.
Martí, J., Pinel, V., López, C., Geyer, A., Abella, R., Tárraga, M., Blanco, M.J., Castro, A., Rodríguez, C., 2013. Causes and mechanisms of the 2011–2012 El Hierro (Canary Islands) submarine eruption. J. Geophys. Res. 118, 1–17.
Martinez-Arevalo, C., Mancilla, F.D.L., Helffrich, G., Garcia, A., 2013. Seismic evidence of a regional sublithospheric low velocity layer beneath the Canary Islands. Tectonophysics 608, 586–599.

Masson, D.G., 1996. Catastrophic collapse of the volcanic island of Hierro 15-ka ago and the history of landslides in the Canary Islands. Geology 24, 231–234.
Masson, D.G., Watts, A.B., Gee, M.J.R., Urgeles, R., Mitchell, N.C., Le Bas, T.P., Canals, M., 2002. Slope failures on the flanks of the western Canary Islands. Earth Sci. Rev. 57, 1–35.
Medialdea, T., Somoza, L., González, F.J., Vázquez, J.T., de Ignacio, C., Sumino, H., Sánchez-Guillamón, O., Orihashi, Y., León, R., Palomino, D., 2017. Evidence of a modern deep water magmatic hydrothermal system in the Canary Basin (eastern Central Atlantic Ocean). Geochem. Geophys. Geosyst. 18, 3138–3164. https://doi.org/10.1002/2017gc006889.
Muck, M.T., Underwood, M.B., 1990. Upslope flow of turbidity currents: a comparison among field observations, theory, and laboratory models. Geology 18, 54–57.
Negredo, A.M., van Hunen, J., Rodríguez-González, J., Fullea, J., 2022. On the origin of the Canary Islands: Insights from mantle convection modelling. Earth Planet. Sci. Lett. 584, 117506 https://doi.org/10.1016/j.epsl.2022.117506.
Palomino, D., Vázquez, J.-T., Somoza, L., León, R., López-González, N., Medialdea, T., Fernández-Salas, L.-M., González, F.-J., Rengel, J.A., 2016. Geomorphological features in the southern Canary Island Volcanic Province: the importance of volcanic processes and massive slope instabilities associated with seamounts. Geomorphology 255, 125–139.
Parker, G., 1982. Conditions for the ignition of catastrophically erosive turbidity currents. Mar. Geol. 46, 307–327.
Paull, C.K., Talling, P.J., Maier, K.L., Parsons, D., Xu, J., Caress, D.W., Gwiazda, R., Lundsten, E.M., Anderson, K., Barry, J.P., Chaffey, M., O'Reilly, T., Rosenberger, K. J., Gales, J.A., Kieft, B., McGann, M., Simmons, S.M., McGann, M., Sumner, E.J., Clare, M.A., Cartigny, M.J., 2018. Powerful turbidity currents driven by dense basal layers. Nat. Commun. 9, 4114. https://doi.org/10.1038/s41467-018-06254-6.
Pellicer, M.J., 1979. Estudio geoquímico del vulcanismo de la isla del Hierro, Archipiélago Canario. Estud. Geol. 35, 15–29.
Pfänder, J.A., Sperner, B., Ratschbacher, L., Fischer, A., Meyer, M., Leistner, M., Schaeben, H., 2014. High-resolution $^{40}Ar/^{39}Ar$ dating using a mechanical sample transfer system combined with a high-temperature cell for step heating experiments and a multicollector ARGUS noble gas mass spectrometer. Geochem. Geophys. Geosyst. 15, 2713–2726. https://doi.org/10.1002/2014GC005289.
Pilet, S., Baker, M.B., Stolper, E.M., 2008. Metasomatized Lithosphere and the Origin of Alkaline Lavas. Science 320, 916–919.
Piper, D.J.W., Cochonat, P., Morrison, M.L., 1999. The sequence of events around the epicentre of the 1929 Grand Bank earthquake: initiation of debris flows and turbidity current inferred from sidescan sonar. Sedimentology 46, 79–97.
Renne, P.R., Mundil, R., Balco, G., Min, K., Ludwig, K.R., 2010. Joint determination of ^{40}K decay constants and $^{40}Ar^*/^{40}K$ for the fish Canyon sanidine standard, and improved accuracy for $^{40}Ar/^{39}Ar$ geochronology. Geochim. Cosmochim. Acta 74, 5349–5367.
Ribe, N.M., Christensen, U.R., 1999. The dynamical origin of Hawaiian volcanism. Earth Planet. Sci. Lett. 171, 517–531.
Risica, G., Di Roberto, A., Speranza, F., Carlo, P.D., Pompilio, M., Meletlidis, S., Todrani, A., 2022. Reconstruction of the subaerial Holocene volcanic activity through paleomagnetic and ^{14}C dating methods: El Hierro (Canary Islands). J. Volcanol. Geotherm. Res. 425, 107526.
Rivera, J., Lastras, G., Canals, M., Acosta, J., Arrese, B., Hermida, N., Micallef, A., Tello, O., Amblas, D., 2013. Construction of an oceanic island: Insights from the El Hierro (Canary Islands) 2011-2012 submarine volcanic eruption. Geology 41, 355–358.
Ryan, W.B.F., Carbotte, S.M., Coplan, J., O'Hara, S., Melkonian, A., Arko, R., Weissel, R. A., Ferrini, V., Goodwillie, A., Nitsche, F., Bonczkowski, J., Zemsky, R., 2009. Global Multi-Resolution Topography (GMRT) synthesis data set. Geochem. Geophys. Geosyst. 10 https://doi.org/10.1029/2008GC002332.
Saal, A.E., Van Orman, J.A., 2004. The ^{226}Ra enrichment in oceanic basalts: evidence for melt-cumulate diffusive interaction processes within the oceanic lithosphere. Geochem. Geophys. Geosyst. 5 https://doi.org/10.1029/2003GC000620.
Santana-Casiano, J.M., Fraile-Nuez, E., González-Dávila, M., Baker, E.T., Resing, J.A., Walker, S.L., 2016. Significant discharge of CO_2 from hydrothermalism associated with the submarine volcano of El Hierro Island. Sci. Rep. 6, 25686. https://doi.org/10.1038/srep25686.
Schmincke, H.-U., Graf, G., 2000. DECOS / OMEX II, Cruise No. 43, 25 November 1998–14 January 1999, METEOR-Berichte. Leitstelle METEOR, Institut für Meereskunde der Universität Hamburg, Hamburg, pp. 1–113. https://doi.org/10.2312/cr_m43.
Scott, S.R., Sims, K.W.W., Reagan, M.K., Ball, L., Schwieters, J.B., Bouman, C., Lloyd, N. S., Waters, C.L., Standish, J.J., Tollstrup, D.L., 2019. The application of abundance sensitivity filters to the precise and accurate measurement of uranium series nuclides by plasma mass spectrometry. Int. J. Mass Spectrom. 435, 321–332.
Sims, K.W.W., Gill, J.B., Dosseto, A., Hoffmann, D.L., Lundstrom, C.C., Williams, R.W., Ball, L., Tollstrup, D., Turner, S., Prytulak, J., Glessner, J.J.G., Standish, J.J., Elliott, T., 2008. An Inter-Laboratory Assessment of the Thorium Isotopic Composition of Synthetic and Rock Reference Materials. Geostand. Geoanal. Res. 32, 65–91.
Sims, K.W.W., Pichat, S., Reagan, M.K., Kyle, P.R., Dulaiova, H., Dunbar, N.W., Prytulak, J., Sawyer, G., Layne, G.D., Blichert-Toft, J., Gauthier, P.J., Charette, M.A., Elliott, T.R., 2013. On the Time Scales of Magma Genesis, Melt Evolution, Crystal Growth rates and Magma Degassing in the Erebus Volcano Magmatic System using the ^{238}U, ^{235}U and ^{232}Th Decay Series. J. Petrol. 54, 235–271.
Stracke, A., Bourdon, B., 2009. The importance of melt extraction for tracing mantle heterogeneity. Geochim. Cosmochim. Acta 73, 218–238.
Stroncik, N.A., Klügel, A., Hansteen, T.H., 2009. The magmatic plumbing system beneath El Hierro (Canary Islands): constraints from phenocrysts and naturally quenched basaltic glasses in submarine rocks. Contrib. Mineral. Petrol. 157, 593–607.
Sun, S.S., McDonough, W.F., 1989. Chemical and isotopic systematics of oceanic basalts: implications for mantle composition and processes. Geol. Soc. Lond. Spec. Publ. 42, 313–345.
Talling, P.J., Cartigny, M.J.B., Pope, E., Baker, M., Clare, M.A., Heijnen, M., Hage, S., Parsons, D.R., Simmons, S.M., Paull, C.K., Gwiazda, R., Lintern, G., Hughes Clarke, J. E., Xu, J., Silva Jacinto, R., Maier, K.L., 2023. Detailed monitoring reveals the nature of submarine turbidity currents. Nat. Rev. Earth Environ. 4, 642–658. https://doi.org/10.1038/s43017-023-00458-1.
Turner, S., Beier, C., Niu, Y., Cook, C., 2011. U-Th-Ra disequilibria and the extent of off-axis volcanism across the East Pacific rise at 9°30′N, 10°30′N, and 11°20′N. Geochem. Geophys. Geosyst. 12 https://doi.org/10.1029/2010GC003403.
Turner, S., Hoernle, K., Hauff, F., Johansen, T.S., Klügel, A., Kokfelt, T., Lundstrom, C., 2015. ^{238}U-^{230}Th-^{226}Ra Disequilibria Constraints on the Magmatic Evolution of the Cumbre Vieja Volcanics on La Palma, Canary Islands. J. Petrol. 56, 1999–2024.
Turner, S., Kokfelt, T., Hoernle, K., Johansen, T.S., Hauff, F., Lundstrom, C., van den Bogaard, P., Klügel, A., 2017. Contrasting magmatic cannibalism forms evolved phonolitic magmas in the Canary Islands. Geology 45, 147–150.
Urgeles, R., Canals, M., Baraza, J., Alonso, B., Masson, D., 1997. The most recent megalandslides of the Canary Islands: El Golfo debris avalanche and Canary debris flow, west El Hierro Island. J. Geophys. Res. 102, 20305–20323.
van den Bogaard, P., 2013. The origin of the Canary Island Seamount Province - New ages of old seamounts. Sci. Rep. 3, 1–7. https://doi.org/10.1038/srep02107.
Viccaro, M., Ferlito, C., Cristofolini, R., 2007. Amphibole crystallization in the Etnean feeding system: mineral chemistry and trace element partitioning between Mg-hastingsite and alkali basaltic melt. Eur. J. Mineral. 19, 499–511.
Völker, D., Reichel, T., Wiedicke, M., Heubeck, C., 2008. Turbidites deposited on Southern Central Chilean seamounts: evidence for energetic turbidity currents. Mar. Geol. 251, 15–31.
Wallace, P.J., Edmonds, M., 2011. The Sulfur Budget in Magmas: evidence from Melt Inclusions, Submarine Glasses, and Volcanic Gas Emissions, in: Behrens, H., Webster, J.D. (Eds.). Rev. Mineral. 73, 215–246.
Wanless, V.D., Garcia, M.O., Trusdell, F.A., Rhodes, J.M., Norman, M.D., Weis, D., Fornari, D.J., Kurz, M.D., Guillou, H., 2006. Submarine radial vents on Mauna Loa Volcano, Hawai'i. Geochem. Geophys. Geosyst. 7 https://doi.org/10.1029/2005GC001086.
Wessel, P., 2001. Global distribution of seamounts inferred from gridded Geosat/ERS-1 altimetry. J. Geophys. Res. 106, 19431–19441.
Willbold, M., Stracke, A., 2006. Trace element composition of mantle end-members: Implications for recycling of oceanic and upper and lower continental crust. Geochem. Geophys. Geosyst. 7 https://doi.org/10.1029/2005GC001005.
Yang, Z.-F., Zhou, J.-H., 2013. Can we identify source lithology of basalt? Sci. Rep. 3, 1856. https://doi.org/10.1038/srep01856.
Zindler, A., Hart, S.R., 1986. Chemical geodynamics. Annu. Rev. Earth Planet. Sci. 14, 493–571.